Local fracture criterion for quasi-cleavage hydrogen-assisted cracking of tempered martensitic steels

L. Cupertino Malheiros, Abdelali Oudriss, S. Cohendoz, J. Bouhattate, F. Thébault, M. Piette, X. Feaugas

Version of Record: https://www.sciencedirect.com/science/article/pii/S0921509322006153
Manuscript_ca6227158f5344d9b27ad7c21dd392f9

Local fracture criterion for quasi-cleavage hydrogen-assisted cracking of tempered martensitic steels

L. Cupertino Malheiros[a,b*], A. Oudriss[a], S. Cohendoz[a], J. Bouhattate[a], F. Thébault[b], M. Piette[b], X. Feaugas[a]

[a] La Rochelle Université, Laboratoire des Sciences de l'Ingénieur pour l'Environnement, UMR CNRS 7356, Avenue Michel Crépeau, 17042 La Rochelle Cedex, France
[b] Vallourec Research Center France, 60 route de Leval, F-59620 Aulnoye-Aymeries, France

*Corresponding author: livia-raquel.cupertinomalheiros@vallourec.com

ABSTRACT

Electrochemical permeation cell built on a Instron tensile testing machine allows fracturing notched specimens under hydrogen flux while monitoring simultaneously the flow stress and the permeation anodic current. Analysis of the fracture surfaces reveals that cracking initiates at the hydrogen-entry surfaces as quasi-cleavage regions followed by ductile propagation. Quasi-cleavage zones were fully developed at the maximum engineering stress and often initiate around inclusions for unnotched specimens. The observation of multiple cracks at the hydrogen-entry surfaces and correlations between quasi-cleavage features and martensitic boundaries suggest that cracking is related to decohesion of cropping out and inner boundaries. The local mechanical states and diffusible hydrogen concentration and flux at quasi-cleavage failure were calculated by finite element method (FEM). The results predict local failure criteria in terms of decrease of local maximum principal stress and equivalent plastic strain with local diffusible hydrogen concentration, revealing that the inclusion of hydrogen-mechanical-structural interactions at the charging surfaces is necessary to complete fracture analysis.

Keywords: Martensitic steel, Hydrogen embrittlement, Hydrogen-assisted cracking, Fracture behavior, Quasi-cleavage, Finite element analysis

1. Introduction

Hydrogen embrittlement comprises all forms of hydrogen-induced degradation in materials, which can be responsible for premature failure of industrial components in service. In the context of oil and gas industry, hydrogen sulfide promotes absorption and diffusion of hydrogen into steels[1-2] causing a risk of cracking of sour service products. Sulfide stress cracking (SSC) is a type of hydrogen-assisted crack that affects mainly high-strength steels, characterized by brittle initiation at the surface and propagation perpendicular to a tensile applied or residual stress.

Tempered martensitic steels are often designed for applications requiring high mechanical strength and SSC resistance. For these steels, it has been observed that diffusible hydrogen rather than strongly trapped causes considerable embrittlement changing the fracture mode from ductile microvoid coalescence to brittle intergranular or quasi-cleavage transgranular fracture.[3-11] Cracking along prior austenite grain boundaries results in intergranular fracture,[3,6,12-14] whereas cracking along packet, block and/or lath martensitic boundaries could lead to the quasi-cleavage morphology. [6,8,11,14-16] The mechanisms by which hydrogen promotes these two modes of fracture are still unclear. Some authors explain the intergranular and quasi-cleavage fractures solely by the hydrogen-enhanced decohesion mechanism (HEDE),[17-19] whereas Nagumo and Matsuda suggest that hydrogen increases the concentration of strain-induced vacancy clusters in the vicinity of boundaries, leading to microcraking or microvoids around them.[6,20] A third hypothesis is that hydrogen-enhanced-plasticity-mediated decohesion is the acting mechanism for hydrogen-assisted intergranular and quasi-cleavage fractures of martensitic steels.[13,14,21,22] Hydrogen would ease dislocations activity (Hydrogen-enhanced localized plasticity, HELP mechanism).[3,23-25] Then the slip bands intersecting boundaries and the hydrogen transported by dislocations[26-28] would

increase hydrogen accumulation to martensitic boundaries, favoring interface decohesion (HEDE mechanism).

In view of the hydrogen-enhanced-plasticity-mediated decohesion mechanism, Nagao *et al.*[14] have used the statistical physical-based micro-mechanical approach of Novak *et al.*[13] to satisfactorily predict the experimental decay of fracture strength with hydrogen. The performed experiments were four-point bending tests with notched specimens pre-charged with hydrogen, whereas the model includes decohesion of prior austenite or blocks boundaries driven by hydrogen deposited by dislocation pile ups.

Independent of the acting mechanism, it is crucial to determine the threshold conditions necessary to the development of hydrogen-assisted cracking in order to classify steels designed to withstand service applications where hydrogen embrittlement resistance is needed. Wang *et al.*[29-31] have approached this challenge by performing slow strain rate testing (SSRT) on notched specimens of a high-strength martensitic steel electrochemically pre-charged with hydrogen. They observed a unique fracture criterion for the various notched geometries represented as a decay of peak maximum principal stress[29, 31] or the equivalent plastic strain at notch root[29] with the local diffusible hydrogen concentration. Afterwards, Ayas *et al.*[32] employed finite element calculations to validate the local fracture criterion in terms of locus peak maximum principal stress and lattice hydrogen concentration proposed by Wang *et al.*[29,31] for SSRT and also for more rapid tensile tests.[33]

Continuing our previous works with a hydrogen electrochemical permeation cell built on a Instron tensile testing machine,[11,34] the present research aims to investigate the local fracture conditions of three tempered martensitic steels tensile tested under constant permeation hydrogen flux. This approach innovates in tensile testing the steels in a design that favors hydrogen flux throughout the specimen's thickness different from other works where specimens were pre-charged and hydrogen desorption was blocked with coatings.[13,14,22,29-31]

Notches were used to modify the stress and strain states, whereas changing the applied cathodic current densities modified the severity of the hydrogen charging. The permeation results provided information about the diffusion kinetics within the steels. The anodic current density together with the load were monitored during the entire tensile tests up to fracture. Fracture surfaces examination and finite element method (FEM) calculations were employed to provide further explanations regarding the local threshold conditions and the mechanisms for quasi-cleavage (QC) hydrogen-assisted cracking of martensitic steels.

2. Experimental procedures

2.1 Material and characterization

The present work studied three tempered martensitic steels, which simplified chemical composition is given in Table 1. The steels also contain similar small quantities (less than 0.04 wt.%) of Cu, Ni, Nb, N, Ti, Ca and Al. The steel named Ref is considered as the reference chemical composition in this research, whereas the other names refer to the higher Mo and V contents of the HMV steel and the higher carbon and vanadium for the HCV one. Samples of 180 x 120 x 15 mm were austenitized for 15 min at 910°C and then water quenched for the Ref and HMV steels. For the higher carbon HCV steel, austenitization was performed during the same time at 850°C and the quenching in oil. Thereafter, tempering was conducted for 30 min at the temperatures indicated in the Table 1. These temperatures were chosen to provide similar levels of yield strength (at the Lüders plateaus) around 920 MPa for the three studied steels. As expected, for the higher carbon (HCV) and more-alloyed (HMV) steels the tempering temperatures to obtain the same strength levels are higher (737 and 715°C) than for the Ref steel.

Table 1: Chemical composition in weight% and tempering temperature for the three studied steels.

Steels	**C**	**Si**	**Mn**	**Cr**	**Mo**	**V**	**Ttempering**
Ref	0.3	0.2	0.4	1.0	0.8	0.00	670°C
HMV	0.3	0.3	0.3	0.5	1.8	0.20	715°C
HCV	0.6	0.3	0.3	1.0	1.2	0.15	737°C

Optical microscopic images of etched samples confirmed the presence of the desired tempered martensitic structure with prior austenite grain around 5 and 4 µm for the Ref and HMV steels estimated by the intercept method. The grain structure of the HCV steels was finer than 4 µm, being difficult to measure the grain size by metallographic analysis. Dislocation density was estimated by the line-intercept method using five TEM images for each steel.[35] Energy-dispersive X-ray spectroscopy (SEM-EDS) analysis identified the nature of inclusions and undissolved carbo-nitrides. Precipitates were characterized by synchrotron X-ray diffraction spectra and TEM diffraction patterns. Energy-dispersive X-ray diffraction (EDXRD) technique was employed to verify the absence of retained austenite. Table 2 summarizes all these structural characterization results for the three studied steels.

Table 2: Structural parameters of the studied steels. PAG is prior austenite grain, ρ dislocation density and RA retained austenite.

Steels	**PAG (µm)**	**ρ (m^{-2})**	**Inclusions**	**Precipitates**	**RA (%)**
Ref	5	4×10^{14}	Al_2O_3, CaO, SiO_2, oxide-sulfides, (Nb,Ti)(C,N)	Cementite, Mo_2C	0.0
HMV	4	3×10^{14}		Cementite, Mo_2C, VC	0.0
HCV	< 4	3×10^{14}		Cementite, Mo_2C, VC	0.4 ± 0.2

Hydrogen diffusion and trapping characterization was performed using electrochemical permeation (EP) and thermal desorption spectroscopy (TDS). Activation energies and number densities of interstitial and trapping sites were obtained using the data of EP tests performed at four different temperatures and TDS conducted at seven distinct heating rates. A detailed description of these methodologies has already been published in previous works.[34,36,37]

2.2. Mechanical tests

Tensile tests up to fracture were performed without hydrogen (or in air), after hydrogen pre-charging and desorption, and under hydrogen flux. Smooth and notched round and flat specimens were used, whose geometries are shown in the Figure 1(a). The external diameter (*De*) of the smooth and V-notched round specimens is 6.35 mm, whereas the U-notched specimens present external diameter of 9 mm. Three U-notches were used, two with internal

diameter (*Di*) of 5 mm and notch tip radius of 5 or 3 mm and another with *Di* of 7 mm and notch tip radius of 1 mm. The round V-notches have *Di* of 4.52 mm, notch tip radius of 0.1 mm and angle of 60° as illustrated in the Figure 1(a). For the flat specimens [Figure 1(a)], the overall thickness is 2.25 mm and at the notches bottom the thickness is 1.25 mm. The U-notch has a radius of 1 mm, whereas the V-notch presents a tip radius of 0.1 mm and angle of 60°. Additionally, small notches (0.8 mm depth and 62.5 mm radius) were machined in both sides of the smooth plate specimens. These notches aim to ensure that the specimens fracture inside of the permeation zone of 20 mm when tested under hydrogen flux affecting less the tensile and fracture behaviors than the U and V notches.

The tensile tests were performed on an electromechanical Instron machine equipped with a 100 kN load cell at strain rate of 10^{-5} s^{-1}. For the pre-charged condition, round specimens were cathodically charged with hydrogen in a H_2SO_4 1 mol/L solution inside a cell as shown in the photo and schematic drawing of Figure 1(b). The cell contains a saturated sulfate SSE ($Hg/Hg_2SO_4/K_2SO_4$) reference electrode in a Luggin capillary and a platinum counter electrode. The temperature was set to 20°C and the cell was deaerated with argon. After 24 hours of hydrogen charging with cathodic polarization from 20 to 100 mA/cm^2, the specimens were left at room temperature for 48 hours allowing diffusible hydrogen desorption before being tensile tested until fracture. Lastly, TDS measurements of the trapped hydrogen concentration after the tensile tests were conducted. For these measurements, samples of approximately 1g were extracted from the specimens just below the fracture surfaces, preserving them for latter observation.

Flat specimens were fractured in air and under hydrogen flux. The tests with hydrogen were conducted in an electrochemical permeation cell assembled on the tensile testing machine as illustrated in the Figure 1(b). The permeation setup contained a two-compartment electrolytic cell equipped with SSE ($Hg/Hg_2SO_4/K_2SO_4$) reference electrodes and platinum counter

electrodes. A floating ground Radiometer galvanostat PGP201 was used in the charging cell, whereas a Radiometer potentiostat PGP201 was employed in the detection cell. Deionized water circulated in the double jacket through a cryothermostat Lauda RK8 CS maintaining a constant temperature of 20°C. Before being poured into the compartments, solutions of both cells were deaerated by argon for one hour. This deoxygenation was maintained throughout the entire tests. At the beginning, the detection sides of the specimens were maintained at a constant potential of -300 mV/SSE in a 0.1 mol/L Na0H solution for around 22 hours in order to stabilize the anodic current density at values approximately equal to 0.1 $\mu A/cm^2$. Then, the charging sides of the specimens were polarized with a constant cathodic current density from 5 to 50 mA/cm^2 in a 1 mol/L H_2SO_4 solution. A Teflon holder with an opening of 20 mm diameter attached the permeation compartments to the flat specimens. Therefore, hydrogen permeation occurred in only 20% of the specimens' gauge length of 90 mm, where the notches are located and fracture developed.

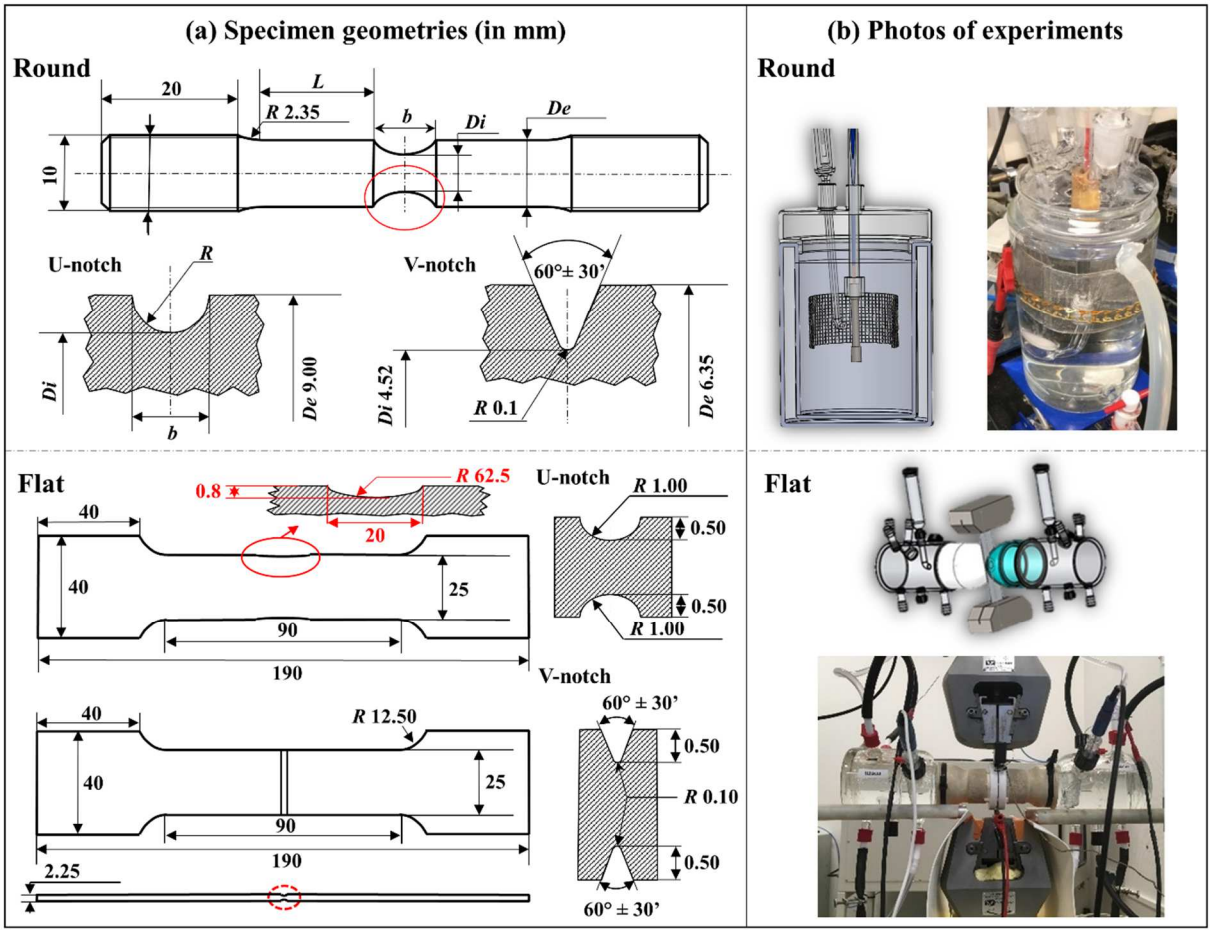

Figure 1: (a) Schematic drawing with dimensions in mm and (b) experimental setups for round and flat tensile specimens. Round is used for hydrogen pre-charged while flat for under hydrogen flux tests.

The tensile tests were started after the permeation reached the steady state where an equilibrium is obtained between the kinetics of diffusive and trapped hydrogen seen as a constant anodic current density indicative of a constant hydrogen flux. During these tests, we continuously monitored the evolutions of stress and anodic current, proportional to the hydrogen flux. A few hours after the end of the tensile tests, samples of around 1g were cut below the fracture surfaces to conduct TDS measurements of the trapped hydrogen concentration. The fracture surfaces of all the tested conditions were later examined using the SEM Philips FEI: Quanta 200FEG/ESEM, 20 kV.

2.3 – Plasticity, diffusion and trapping models

Finite element method (FEM) was used for all the specimens' geometries [Figure 1(a)]. The calculations were computed with the software COMSOL Multiphysics to provide mechanical

and hydrogen distribution within the bulk up to fracture, assuming J_2 flow theory with isotropic and kinematic hardening[38] and diffusion-trapping model.[39] During loading, the mesh is reorganized to take into account the displacement. An elastoplastic law is identified from the plastic behavior of the alloy before necking in the framework of the classical elastoplastic theory.[38,40] The validity of the FEM calculations was checked by comparing the calculated tensile curves and reductions of section with the experimental values.

The effect of hydrostatic stress (σ_m) on the diffusion equation is a well-known process,[39,41-43] which is included in our calculation to evaluate the impact of the mechanical state in the hydrogen distribution for all the tested conditions. The set of employed equations is briefly described below.

Plasticity equations – The elastoplastic law was identified within the framework of the classical elastoplastic theory, based on the thermodynamics of irreversible processes with internal variables.[38,44] The stress was computed from the total strain (ε) and the plastic strain (ε^p) through the Hooke's law (Equation 1), where C is the fourth-order elastic stiffness tensor:

$$\sigma = C{:}(\varepsilon - \varepsilon^p) \tag{1}$$

The yield criterion was written as:

$$f(\sigma) \coloneqq J_2 - k - R = \sqrt{\frac{3}{2} s{:}s} - k - R = 0 \tag{2}$$

Where s is the deviatoric part of the stress tensor σ, k is the yield stress and R a sum of hardening contributions calculated as a function of the equivalent plastic strain (p) and empirical constants (Q_i, b_i):

$$R = \sum_{i=1}^{3} (Q_i / b_i) * \left(1 - e^{-b_i p}\right) \tag{3}$$

Lastly, the plastic strain rate was calculated by Equation 4, where λ is a plastic multiplier (nonnegative scalar).

$$\dot{\varepsilon}^{\mathrm{p}} = \lambda \frac{\partial f(\sigma)}{\partial \sigma} \tag{4}$$

The mechanical behavior was defined using nine parameters E, ν, k, Q_1, Q_2, Q_3, b_1, b_2 and b_3. E and ν are equal to 200 ± 10 GPa and 0.3 for the three studied steels. Table 3 displays the values of the other parameters with the respective deviations for each steel, obtained by trial-and-error method, through successive calculations until satisfactory fitting the experimental tensile curves and reductions of section. The need of slightly modify the parameters is linked to experimental uncertainties and also to the fact that the employed elasto-plastic law does not consider the Lüders band phenomenon, complicating the modeling of the experimental tensile curves, especially for unnotched specimens.

Diffusion and Trapping equations – In the present work, we consider the contributions of deeply trapped hydrogen (C_{Tir}) and lattice hydrogen (C_{L}) to the diffusion. The employed equations are simplifications of diffusion and trapping models described in previous works:[39,45]

$$J(C_{\mathrm{D}}, \sigma_{\mathrm{m}}) = -D_{\mathrm{app}} \left(\frac{\partial C_{\mathrm{D}}}{\partial x} - \frac{\mathrm{V_H}}{\mathrm{RT}} C_{\mathrm{D}} \frac{\partial \sigma_{\mathrm{m}}}{\partial x} \right) \text{ where } D_{\mathrm{app}}(x,t) = D_{\mathrm{L}} / \left(1 + \frac{\partial C_{\mathrm{T}}}{\partial C_{\mathrm{L}}} \right) \tag{5}$$

And

$$C_{\mathrm{T}}(x,t) = N_{\mathrm{T}} / 1 + \frac{N_{\mathrm{L}}}{K_{\mathrm{T}} C_{\mathrm{L}}(x,t)} \text{ with } K_{\mathrm{T}} = \exp\left[\frac{-\Delta E_{\mathrm{T}}}{\mathrm{k_B T}} \right] \tag{6}$$

D_{L} is the interstitial diffusion coefficient, D_{app} is the apparent diffusion coefficient, ΔE_{T} is the trap binding energy, K_{T} is a constant related to the trapping energy, $\mathrm{k_B}$ is the Boltzmann constant, T is the temperature, $\mathrm{V_H}$ is the partial molar volume of hydrogen (considered 2 x 10^{-6} $\mathrm{m^3/mol}$),[45] N_{T} and N_{L} are the number density of trapping and interstitial sites. The model presents only two hydrogen states, trapped (C_{T}) and diffusible (C_{D}), i.e., it does not distinguish the lattice hydrogen (C_{L}) from the reversible trapped hydrogen (C_{Tr}). For the equations 5 and 6, it was considered $C_{\mathrm{L}} = 0.05 C_{\mathrm{D}}$, based on the electrochemical permeation

observations that C_L corresponds to less than 5% of the sub-surface concentration (C_0). This consideration provides D_{app} values similar to the average experimental ones displayed in Table 3. The diffusion/trapping behavior of each steel is defined using the four parameters D_L, N_L, N_T and ΔE_T, whose experimental values obtained from EP and TDS data are also shown in Table 3.

Table 3: Values of the parameters used in the plasticity and hydrogen diffusion and trapping models.

Plasticity							
Steels	***k* (MPa)**	***Q1* (GPa)**	***Q2* (GPa)**	***Q3* (GPa)**	***b1***	***b2***	***b3***
Ref	842 ± 11	2.31 ± 0.06	0.86 ± 0.03	0.83 ± 0.03	26.3 ± 2.3	10.6 ± 0.5	6.0 ± 0.9
HMV	847 ± 8	1.97 ± 0.03	0.86 ± 0.02	0.83 ± 0.02	27.6 ± 1.6	11.9 ± 1.2	6.9 ± 0.9
HCV	841 ± 10	1.50 ± 0.00	0.88 ± 0.00	0.85 ± 0.00	26.4 ± 0.8	7.1 ± 0.8	4.8 ± 0.5
Diffusion and Trapping							
Steels	**D_{app} (m^2/s)**		**D_L (m^2/s)**	**N_L (m^{-3})**	**N_T (m^{-3})**	**ΔE_T (eV)**	
Ref	4.9×10^{-11}		1.2×10^{-9}	3.2×10^{29}	1.6×10^{25}	0.33	
HMV	2.1×10^{-11}		2.0×10^{-9}	6.1×10^{30}	1.7×10^{26}	0.38	
HCV	5.3×10^{-11}		2.6×10^{-9}	9.2×10^{28}	2.1×10^{25}	0.31	

The D_{app} values of the three steels are in the range expected for low-alloy tempered martensitic steels (around 10^{-11} m^2/s).[34,36,47] Among them, the HMV steel presents the slowest hydrogen diffusion kinetics mostly associated to its higher density of trapping sites (N_T), which was later linked to the precipitation of vanadium carbides a few nanometers in size observed by TEM images and diffraction patterns. The other two steels did not present such fine precipitates and have similar hydrogen diffusion kinetics.

3. Results

3.1 Mechanical tests

Table 4 presents the test conditions for the several round specimens with their respective stress concentration factors (*Kt*) and measured irreversible hydrogen trapped concentration (C_{Tir}) by TDS after fracture. For each condition, the maximum engineering stress (σ_{max}), fracture stress (σ_F), total elongation (El_T) and local plastic strain associated to the reduction of section (ε_{loc} calculated by Equation 7) are displayed.

$$\varepsilon_{\mathrm{loc}} = \left[- \ln\left(\frac{section_{\mathrm{f}}}{section_0}\right)\right] * 100 \quad (7)$$

Table 4: Fracture conditions (σ_{max}, σ_F, El_T, ε_{loc}) and hydrogen trapped concentration (C_{Tir}) for round specimens tested in air or after pre-charging and desorption (PC). Stresses are given in MPa and hydrogen concentration in wppm.

Steel	*Kt*	Test	C_{Tir}	σ_{max}	σ_F	El_T (%)	ε_{loc} (%)
Ref	1	Air	0	966	533	16.6	128
	1	PC 100 mA/cm^2 & 48h desorption	0.4	966	523	17	131
	1	PC 100 mA/cm^2 & 0.5h desorption	-	962	540	17	125
	1.3	Air	0	1163	813	13.6	81
	1.3	PC 100 mA/cm^2 & 48h desorption	0.4	1171	813	13.4	129
	1.5	Air	0	1194	911	10.3	71
	1.5	PC 100 mA/cm^2 & 48h desorption	0.4	1195	903	10.0	75
	4.2	Air	0	1397	892	6.3	35
	4.2	PC 20 mA/cm^2 & 48h desorption	0.2	1382	818	6.3	36
HMV	1	Air	0	961	599	15.5	108
	1	PC 20 mA/cm^2 & 48h desorption	1.5	965	605	15.3	111
	1	PC 100 mA/cm^2 & 0.5h desorption	-	968	625	15.0	102
	1.3	Air	0	1135	851	11.7	74
	1.3	PC 20 mA/cm^2 & 48h desorption	1.0	1135	859	11.5	68
	2.1	Air	0	1297	890	14.6	55
	2.1	PC 20 mA/cm^2 & 48h desorption	0.7	1311	917	14.6	55
	4.2	Air	0	1400	941	5.4	35
	4.2	PC 20 mA/cm^2 & 48h desorption	1.7	1394	923	5.3	30
HCV	1	Air	0	938	691	17.6	88
	1	PC 100 mA/cm^2 & 48h desorption	0.4	928	674	16.6	91
	1	PC 100 mA/cm^2 & 0.5h desorption	0.4	934	683	17.9	86
	1.3	Air	0	1135	949	10.8	63
	1.3	PC 20 mA/cm^2 & 48h desorption	0.2	1124	936	10.9	65
	1.5	Air	0	1220	1068	7.7	56
	1.5	PC 50 mA/cm^2 & 48h desorption	0.3	1217	1077	7.2	55
	4.2	Air	0	1393	873	3.6	24
	4.2	PC 100 mA/cm^2 & 48h desorption	0.3	1414	997	3.9	29

The tensile curves of the Ref steel are displayed in Figure 2. There were no considerable differences between the pre-charged and air tensile results for the three studied steels. Even the pre-charged smooth curves with only 0.5 hour of hydrogen desorption before tensile testing showed no evidence of embrittlement. All the fracture surfaces were entirely ductile with bimodal-size distributions of microvoids, with the larger ones often around inclusions as illustrated in Figure 2.

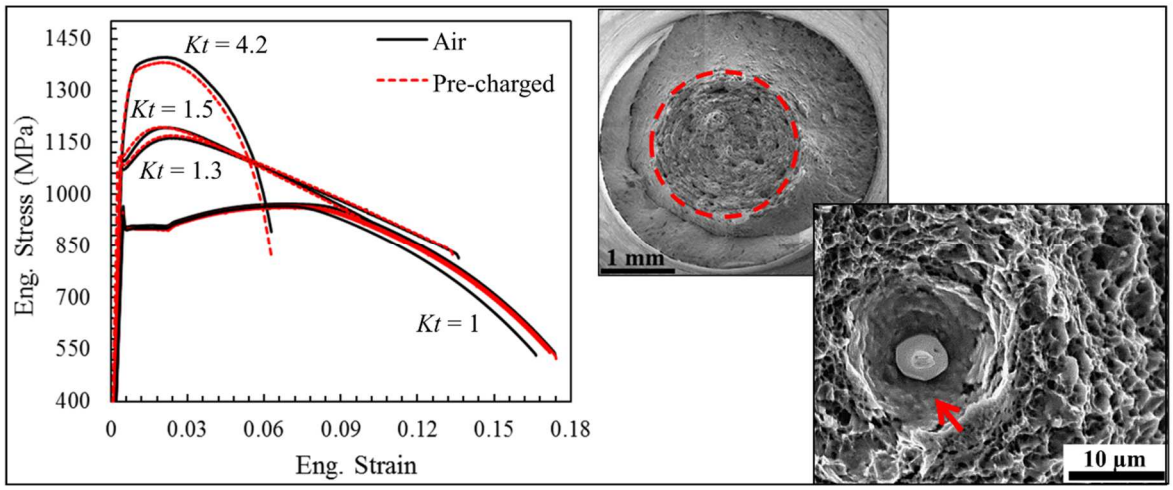

Figure 2: Tensile curves without hydrogen (in black) and after hydrogen pre-charging and desorption (in red) for the Ref steel with an example of ductile fracture surface showing a global view and microvoids. A red arrow indicates an inclusion inside a large void.

On the other hand, the embrittlement effect of hydrogen was observed in all the tests performed under hydrogen flux. Table 5 summarizes the fracture results for these tests for the various geometries (represented by Kt) of flat specimens. The applied cathodic current density, the steady-state hydrogen flux (J_{max}), the sub-surface (C_0) and the trapped hydrogen concentration (C_{Tir}) measured by TDS after around 3 hours of the end of the test are also displayed.

Table 5: Fracture conditions (σ_{max}, σ_F, El_T, ε_{loc}), hydrogen steady-state flux (J_{max}), sub-surface (C_0) and trapped hydrogen concentration (C_{Tir}) for flat specimens tested in air or under hydrogen flux. Stresses are given in MPa, hydrogen flux in µA/cm² and concentration in wppm.

Steel	Kt	Test	J_{max}	C_0	C_{Tir}	σ_{max}	σ_F	El_T (%)	ε_{loc} (%)
Ref	1.1	Air	-	0	0	1001	788	7.4	79
	1.1	Flux 5 mA/cm²	0.3	0.2	-	984	835	5.7	46
	1.1	Flux 20 mA/cm²	0.7	0.4	1.9	1006	837	6.6	39
	1.1	Flux 50 mA/cm²	2.0	0.9	2.1	999	693	6.7	44
	1.4	Air	-	0	0	1338	1268	0.61	22
	1.4	Flux 5 mA/cm²	0.7	0.3	0.1	1312	1242	0.52	12
	1.4	Flux 20 mA/cm²	1.3	0.7	0.1	1327	1281	0.46	7
	1.4	Flux 50 mA/cm²	2.4	1.0	0.3	1284	1257	0.42	5
	3.2	Air	-	0	0	1452	1313	0.89	23
	3.2	Flux 5 mA/cm²	0.5	0.3	0.0	1374	1242	0.67	16
	3.2	Flux 20 mA/cm²	1.3	0.6	0.1	1321	1193	0.68	12
	3.2	Flux 50 mA/cm²	3.5	1.3	0.4	1256	1143	0.6	8
HMV	1.1	Air	-	0	0	973	788	7.6	77
	1.1	Flux 5 mA/cm²	0.2	0.5	1.4	964	829	4.4	36
	1.1	Flux 20 mA/cm²	0.8	1.4	2.6	976	842	6.6	33

	1.1	Flux 50 mA/cm^2	1.1	1.6	2.2	986	822	6.6	37
	1.4	Air	-	0	0	1301	1251	0.56	18
	1.4	Flux 5 mA/cm^2	0.6	1.1	1.5	1264	1213	0.45	7
	1.4	Flux 20 mA/cm^2	0.4	0.5	1.0	1255	1238	0.38	1
	1.4	Flux 50 mA/cm^2	1.0	1.0	2.2	1264	1235	0.41	4
	3.2	Air	-	0	0	1422	1334	0.66	23
	3.2	Flux 20 mA/cm^2	0.4	0.6	1.3	1280	1190	0.57	16
	3.2	Flux 50 mA/cm^2	1.1	1.2	-	1319	1195	0.60	18
HCV	1.1	Air	-	0	0	951	882	6.4	38
	1.1	Flux 5 mA/cm^2	0.3	0.1	0.7	948	789	5.7	32
	1.1	Flux 20 mA/cm^2	1.3	0.6	2.1	955	836	4.8	29
	1.1	Flux 50 mA/cm^2	1.4	0.6	1.4	958	840	4.0	19
	1.4	Air	-	0	0	1297	1258	0.58	15
	1.4	Flux 5 mA/cm^2	0.3	0.1	0.3	1218	1183	0.48	8
	1.4	Flux 20 mA/cm^2	1.5	0.6	0.3	1227	1191	0.47	3
	1.4	Flux 50 mA/cm^2	2.0	0.7	0.3	1192	1156	0.44	3
	3.2	Air	-	0	0	1384	1320	0.62	15
	3.2	Flux 5 mA/cm^2	0.4	0.2	0.3	1281	1169	0.60	11
	3.2	Flux 20 mA/cm^2	1.4	0.7	0.2	1293	1198	0.58	10
	3.2	Flux 50 mA/cm^2	1.9	0.7	0.5	1305	1187	0.62	8

In general, both hydrogen flux and sub-surface concentration increased with the applied cathodic current density for the three studied steels from around 0.2 µA/cm^2 and 0.2 wppm up to the values of 3.5 µA/cm^2 and 1.6 wppm. For the same applied cathodic density, the diffusion and trapping behavior of the steels determines the hydrogen flux (J_{max}) and sub-surface concentration (C_0) at the onset of the tensile tests. It was observed that the Ref and HCV tend to possess higher hydrogen flux and lower subsurface concentration than the HMV steel (the one with superior density of trapping sites).

Figure 3 compares the irreversible trapped hydrogen concentration measured by TDS ($C_{Tir\text{-}TDS}$) after desorption steps of electrochemical permeation of stress-free samples with the values measured after more than 3 hours of the fractures under hydrogen flux. It is possible to see a considerable gap between those values represented by a dashed red line for the specimens with *Kt* equal to 1 or 1.1 fractured under flux compared to the smaller $C_{Tir\text{-}TDS}$ values for the other test conditions. The specimens without notches (*Kt* = 1) or with small notches (*Kt* = 1.1) are the ones with superior levels of plastic strain before fracturing. This result supports the idea that plastic strain increases hydrogen trapping for these steels that can

be related to the increase of dislocation density only, but also to strain-induced vacancies and/or damage.

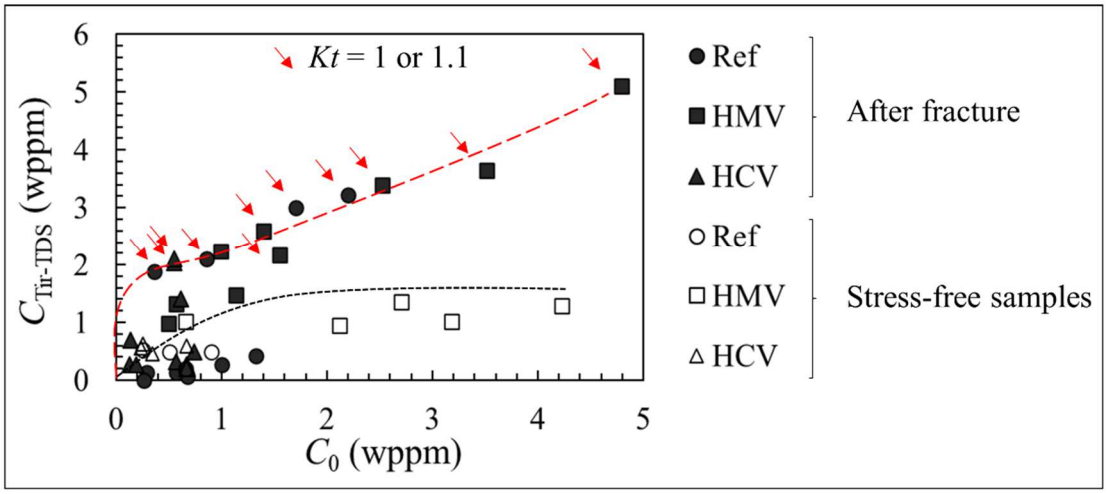

Figure 3: Evolutions of trapped hydrogen concentrations measured by TDS after the desorption step of permeations with stress-free samples (in white) and after some hours of the end of the tensile tests (in black) for the Ref, HMV and HCV steels. Red arrows indicate the specimens with *Kt* equal to 1 or 1.1.

Hydrogen flux modified the tensile curves for the three steels for all the cathodic current densities and specimen geometries. Examples of engineering tensile curves of tests under hydrogen flux are shown together with the ones performed without hydrogen (in air) in the Figure 4 for the Ref steel. For the specimens with *Kt* = 1.1, which are the only ones whose notches are not in the entry and exit surfaces of the hydrogen permeation, hydrogen flux did not considerably affect the stress levels at beginning of plasticity but promoted earlier fracture with total elongations significantly smaller. For the U and V-notched specimens (*Kt* equal to 1.4 and 3.2), hydrogen flux reduced the maximum stresses and total elongations considerably.

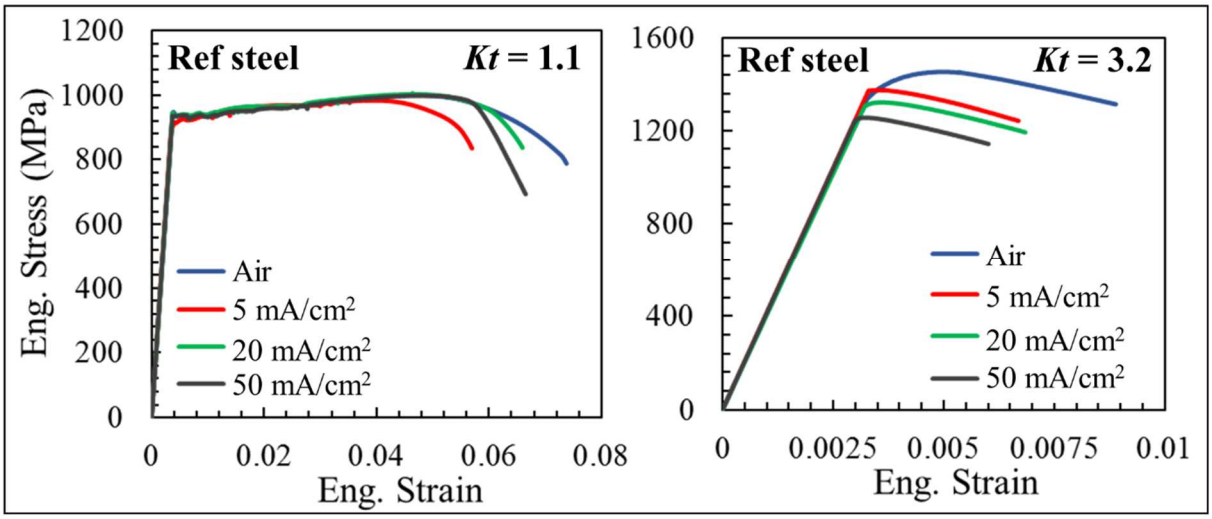

Figure 4: Tensile curves in air and under hydrogen flux (5, 20, 50 mA/cm^2) for specimens with *Kt* equal to 1.1 and 3.2 for the Ref steel.

Further analysis of the effect of hydrogen flux on fracture was completed by fracture surface analysis, which revealed that mobile hydrogen promoted quasi-cleavage (QC) fracture for all the employed geometries and cathodic polarizations. The locations and shapes of the QC zones varied with the specimen geometry but not between the steels. For the specimens with *Kt* = 1.1, without notches at the hydrogen entry and exit sides, QC was observed as elliptical fish-eye zones near the hydrogen entry charging surfaces as can be seen in the Figure 5(a). For most of the samples, multiple QC initiation zones could be noticed along the 20 mm opening of the holder. The biggest fish-eyes have depths of 10 to 50% of the specimen thickness and widths from 0.5 to 2 mm. More detailed SEM imaging of these initiation zones revealed that QC cracking often happened around inclusions or undissolved carbides, such as Al_2O_3 and (Nb, Ti)(C,N) particles, as illustrated in the Figure 5(a). On the other hand, for the U and V specimens (*Kt* = 1.4 and 3.2), with notches at both hydrogen charging and detection sides, QC zones with nearly constant thickness, covering almost the entire specimens' width under hydrogen flux (20 mm opening of the holder) were observed again next to the hydrogen entry sides as shown in an example in Figures 5(a). The edges of the specimens (2.5 mm of each side) outside the opening of the permeation holder presented ductile fracture throughout

their thickness, even at the notch tips at the hydrogen entry surfaces. These QC bands have depths of 6-15% and 19-35% of the specimen thickness for the U and V specimens, respectively. It is important to notice that QC only occurred at the exit detection side for one V specimen (Kt = 3.2) of the Ref steel tested at the highest cathodic current density of 50 mA/cm^2. This QC band presented depth of around 4% of the specimen thickness. For all the other tests under hydrogen flux, quasi-cleavage was only observed next to the entry charging sides with the rest of the fracture presenting ductile microvoids morphology.

Figure 5(b) shows in more detail the QC fracture for the Ref and HCV steels. The sizes of the QC features were similar for the Ref and HMV steels, whereas significantly finer for the HCV steel, which presents finer microstructure according to metallographic analysis. Additionally, images of the entry surfaces for all the tested conditions presented multiple cracks as shown in the Figure 5(c). In addition to few-millimeters crack networks, there were also smaller microscopic cracks. Inside of these cracks, it was possible to verify the presence of the same QC morphology, indicating that they are similar to the ones that have propagated causing the brittle fracture of the steels. Finally, there were also voids probably linked to inclusions or undissolved carbides at the charging surfaces with cracks initiating from them.

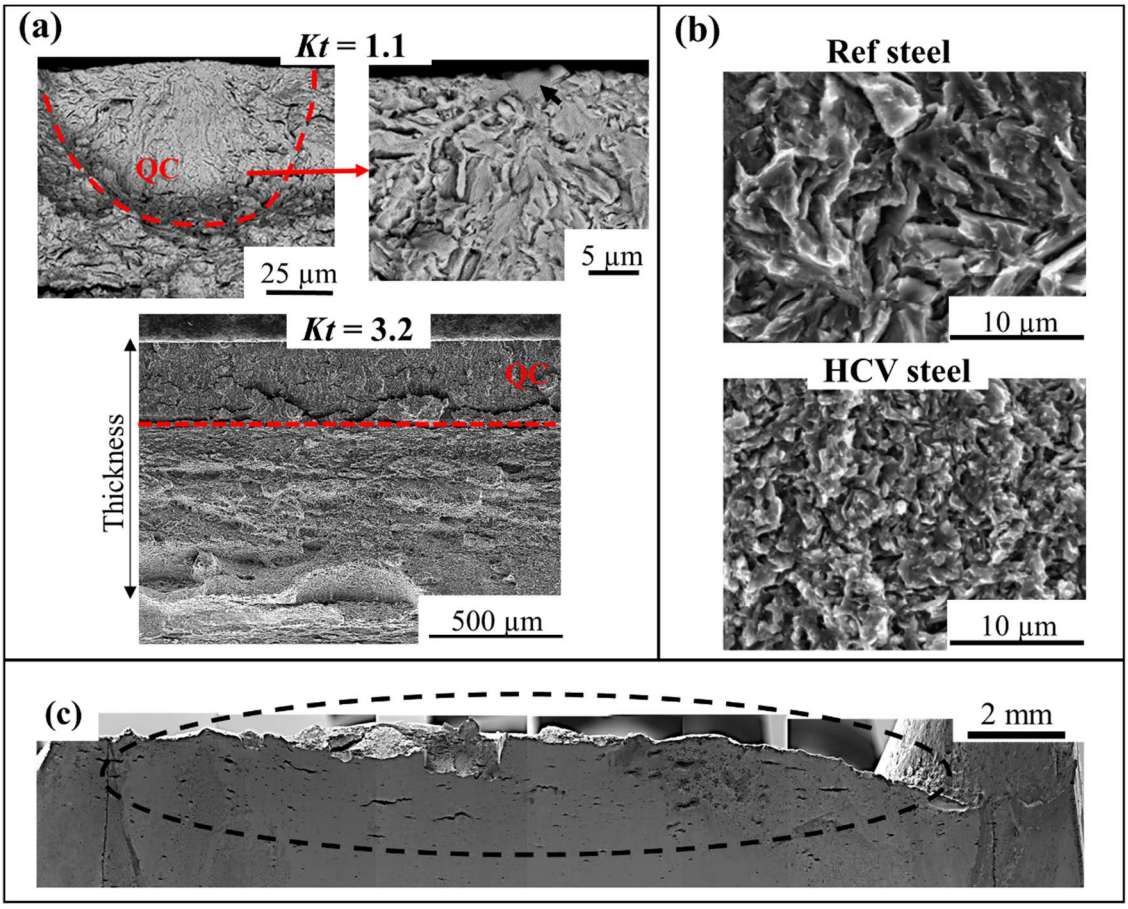

Figure 5: SEM fracture surface images showing (a) QC zones for HMV steel specimens with *Kt* equal to 1.1 and 3.2, (b) QC features for the Ref and HCV steels, (c) multiple cracks at the hydrogen entry surface of a *Kt* 1.1 HMV specimen. Black arrow indicates a (Nb,Ti)(C,N) particle.

An important question regarding the quasi-cleavage is in which moment of the tensile tests this fracture has developed. In order to address this question, a tensile test for the Ref steel V-notched specimen with applied current density of 20 mA/cm^2 was stopped just after the tensile curve reached its maximum stress and broken with liquid nitrogen as illustrated in the tensile curves of the Figure 6. A crack with opening around 0.16 mm could be seen at the bottom of the notch at the hydrogen entry surface. After breaking the specimen, SEM image of fracture revealed a quasi-cleavage zone of 0.37 mm. This value is very similar to the QC thickness obtained for the test 2 until fracture (0.34 mm), indicating that the QC zone was already entirely developed at the maximum engineering tensile stress. By comparing the final thicknesses of the specimens 1 and 2, it is also possible to notice that most of the reduction of

section occurred throughout the ductile propagation that happened during the reduction of stress in the tensile curves.

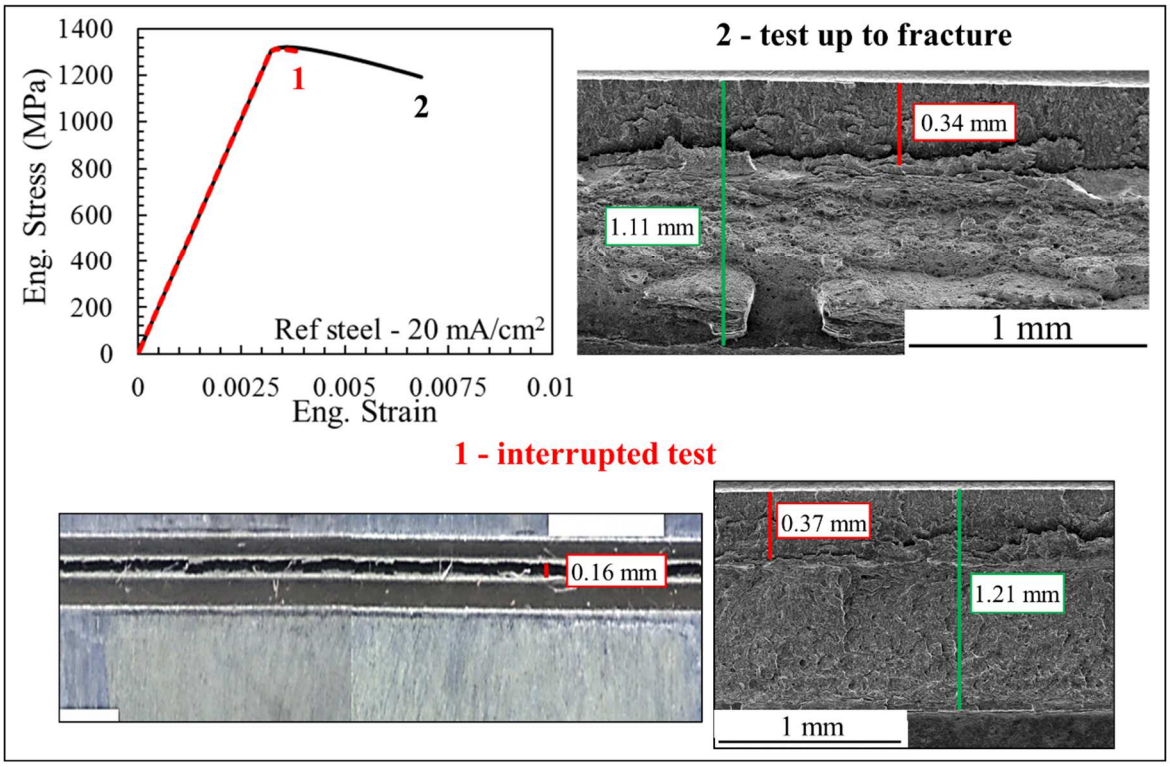

Figure 6: Tensile curves of the Ref steel V specimens tested with 20 mA/cm^2 and stopped just after the maximum stress (test 1 in red) and until fracture (test 2 in black). View of crack at the notch tip at the hydrogen charging side of test 1 and fracture surfaces for the tests 1 and 2. Red lines refer to the QC cracks and green lines to the entire specimen thicknesses.

The permeation assembly on the tensile testing machine allows monitoring the evolution of the anodic current density at the exit side of the permeation during the mechanical tests under hydrogen flux. Changes on this current can be associated to hydrogen flux and/or to plastic strain. The latter may modify the exit surface activity contributing to an increase of the anodic current. In order to separate these two contributions, the first tensile tests were performed without cathodic polarization, with only the monitoring of the anodic current related to the surface activity of the detection side. Thereafter, their anodic current variations were compared to the tests completed under hydrogen flux. The tests without cathodic polarization (without hydrogen) started after the formation of a stable passive film at the detection side, i.e., J around 0.1 µA/cm^2 following more than 20 hours of constant potential (-300 mV/SSE)

in a 0.1 mol/L NaOH solution. It was possible to notice that J varied during the tensile tests for the three steels with a peak during their Lüders bands and an increase after it, when the generalized plastic deformation occurred. On the other hand, for the tests with hydrogen flux, the permeations were conducted in the non-deformed specimens and the tensile tests started when the permeations reached the stationary state ($J \approx$ constant $\approx J_{max}$). In this case, it was possible to observe similar peaks at the Lüders bands followed by drastic reductions of the anodic current densities. These losses of the anodic signal at the exit surfaces after the Lüders band peaks happened even though there were not considerable variations of the cathodic polarization potentials at the entry surfaces, indicating that hydrogen continued to enter the specimens. Figures 7(a) provides an example of these variations of the anodic current density (J) during a tensile test without cathodic polarization and a test cathodically polarized with 50 mA/cm^2 for the Ref steel.

In order to investigate further the sharp decreases of the anodic current at the Lüders bands, two additional tests were conducted and their results are displayed in Figure 7(b). For the first one, the evolutions of J and stress are plotted as function of time and the tensile test with the Ref steel (50 mA/cm^2) started as usual at the stationary state of the permeation. However, after the sharp decrease of the anodic current the tensile testing machine was stopped keeping the total strain constant (time a in the chart). It is possible to see that the anodic current density started to increase reaching a maximum around 6 hours after the tensile machine has been stopped, indicating a saturation of the defects that might be created during the slip bands impeding hydrogen permeation. Then the current slightly reduced until the machine is restarted (time b in the graph). Curiously, the plastic strain caused another sharp decrease of the current that reduced until the specimen fracture. The time scale in this graph may give the false impression that the tensile curve has been affected by hydrogen, which is not the case. This test presented the same total strain (around 10%) than the ones of Figure 7(a). The

relaxed stress (σ^*) during the time the machine is stopped is also indicated in the chart. In the second test, a specimen of the HMV steel (10 mA/cm^2) was tensile loaded until the end of the Lüders plateau and then unloaded to zero before the permeation test. Then the permeation test was performed up to the stationary state and only when the hydrogen flux reached its maximum constant value, the specimen was reloaded until fracture. In this case, there was no drop in anodic current density. The current only increased at the onset of plastic strain of about 1 μA/cm^2. This increase is associated to the disturbance of the passive film due to plastic strain and may have had an extra contribution related to hydrogen transport by mobile dislocations. It is important to notice that the unnotched specimens of Figure 7 fractured outside the 20 mm diameter permeation zones. This is the reason why no hydrogen embrittlement effect is observed in the tensile curves.

Hydrogen flux did not modify the flow stress, except for hardening peaks at the Lüders plateaus, as indicated with a black dashed circle in the chart of Figure 7(a) polarized with 50 mA/cm^2. The results indicate that when the Lüders bands passed through the permeation zones there were breakdown of the passive films with hydrogen impeding the slip bands propagation, causing simultaneous stress and anodic current peaks. These hardening peaks varied from 11 to 19 MPa and were more prominent for the Ref and HMV steels.

Finally, for all the tensile testing under hydrogen flux with notched specimens, where fracture happened inside the permeation zone of 20 mm diameter, the anodic current remained constant until about the maximum values of engineering stress and then rapidly increased. The *J* values continued to increase until the specimens fractured to very high current densities of up to 50 μA/cm^2. Both ductile and brittle fractures can modify the specimen surfaces due to plastic deformation and necking or crack opening and propagation, being able to cause the observed growths of *J*. Therefore, the moment when the anodic current starts to increase can be an indication of the stress level in which the fracture process has started. These results

agree with the observation of Figure 6 that QC developed around the engineering maximum stress.

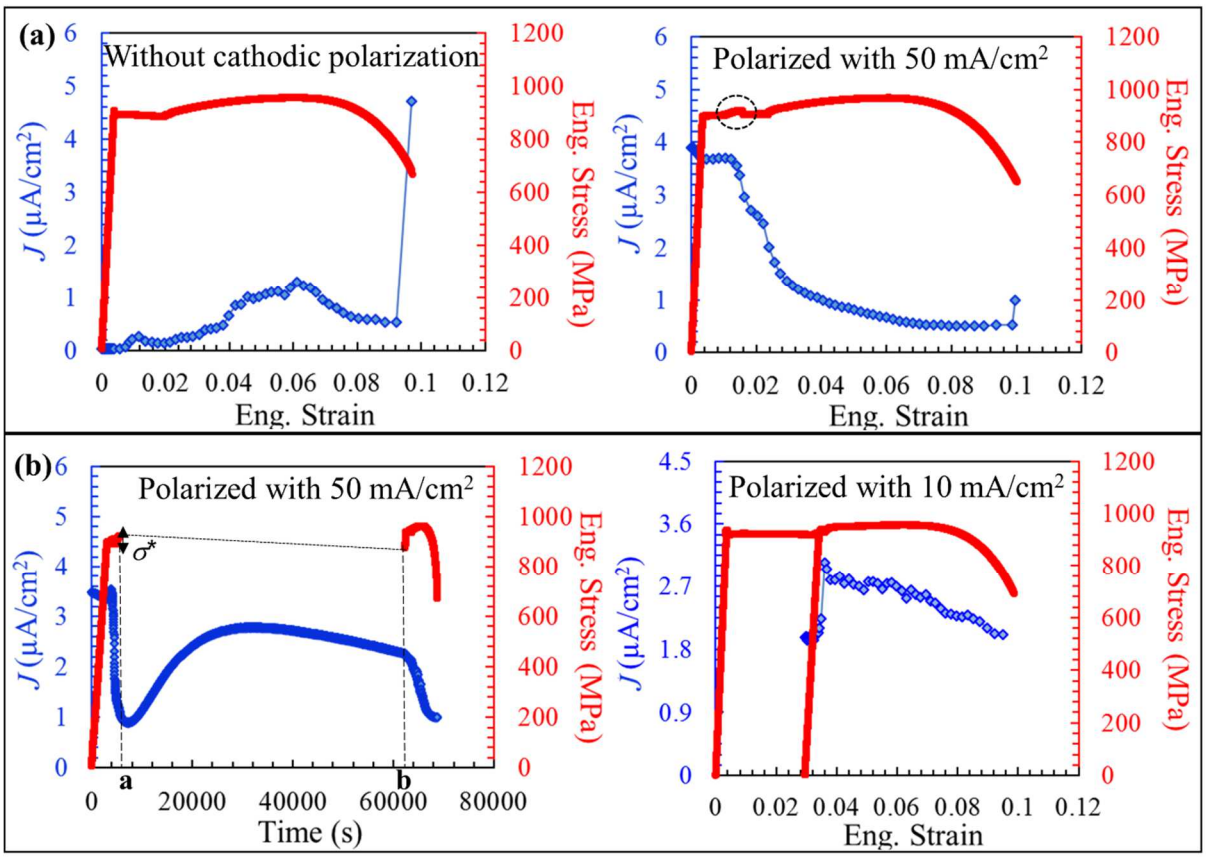

Figure 7: Evolutions of anodic current density (blue lozenges) and engineering stress (red) for unnotched specimens (*Kt* of 1): (a) Ref steel without cathodic polarization and polarized with 50 mA/cm^2, (b) interrupted test for Ref steel polarized with 50 mA/cm^2 and test under flux after passing Lüders plateau for HMV steel polarized with 10 mA/cm^2.

3.2 Local fracture criterion

FEM simulations of the tensile curves provided distributions of mechanical parameters in the bulk of the specimens during loading. We used then the calculated mechanical parameters (principal stresses, hydrostatic stress, von Mises equivalent stress and plastic strain) at the highly solicited regions of the specimens for the corresponding experimental fracture strains to predict the local conditions of fracture. For the tests in air with unnotched and U specimens, the parameter values were taken at the center of the specimens, whereas for the V specimens the employed values were from the sub-surface (below the notch tip).

The initial analysis of the FEM results regards ductile fracture. The voids evolution during a ductile damage depends on the stress state that presents hydrostatic and deviatoric parts, which control the voids growth and shape, respectively. The hydrostatic and deviatoric stresses can be described by the triaxiality (χ equal to the ratio of the hydrostatic stress to the von Mises equivalent stress) and the Lode angle parameter ($\bar{\theta}$), obtained by Equation 8 where ξ is the normalized third stress invariant and σ_1, σ_2 and σ_3 the principal stresses. According to this definition, $\bar{\theta}$ varies from -1 (axisymmetric compression) to 1 (axisymmetric tension).[48-49]

$$\bar{\theta} = 1 - \frac{2}{\pi}\arccos(\xi) \cong -L \quad \text{where} \quad L = \frac{2\sigma_2 - \sigma_1 - \sigma_3}{\sigma_1 - \sigma_3} \tag{8}$$

Based on the values of Lode angle parameter, the specimens could be divided into two groups, the ones with $\bar{\theta}$ closer to 1 and the others with $\bar{\theta}$ around 0. This division corresponds to the round ($\bar{\theta} \approx 1$) and the flat ($\bar{\theta} \approx 0$) specimens, except for the V round specimens which have $\bar{\theta}$ around 0.3. These results indicate that changing the specimen geometry from round to flat favored plane stress conditions and generalized shear.

The models of ductile fracture criterion often consider the voids growth as function of the stress triaxiality (χ) and the von Mises equivalent plastic strain ($\varepsilon_{\text{eqVM}}$).[50-51] Figure 8(a) shows the evolution of $\varepsilon_{\text{eqVM}}$ with χ separated into (a.i) round specimens with Lode angle parameter next to 1 including the V specimens and (a.ii) flat specimens with Lode angle around 0. It is possible to see differences between the resistances of the steels to ductile fracture that happened in this work for the tests without hydrogen or only with deeply trapped hydrogen. The data for the HCV steel are shift towards lower values of equivalent plastic strain and stress triaxiality. On the other hand, the Ref steel presents slightly higher values of plastic strain and triaxiality, especially for the round specimens. These results are a consequence of the greater necking development for the Ref and smaller reductions of section for the HCV

steel. The differences between the steels become smaller as the stress triaxiality increases (specimens with higher *Kt*).

For the quasi-cleavage fracture, mobile hydrogen promoted earlier fracture reducing the total elongation for all the specimens and the maximum stress for the U and V notched ones as previously seen in Figure 4. Additionally, the experiment of Figure 6 showed that QC cleavage crack develops at the maximum stresses for V specimens. In order to simulate these effects of hydrogen, we stopped the FEM computations at lower values of displacements to reproduce the local mechanical conditions during the initiation of QC fracture. The calculations were then stopped at the strains where the curves of the tests under hydrogen flux deviate from the experimental tensile curves in air, which coincided to the maximum engineering stresses for the U and V specimens. Thereafter, the local fracture mechanical parameters were taken from the locations where there are the highest hydrostatic stresses inside the QC zones near the hydrogen entry surfaces. For the *Kt* 1.1 specimens, it was considered the biggest fish-eye as initiation region. These local values were then used to obtain the fracture criterion charts of Figure 8(b). Mobile hydrogen decreased the fracture local equivalent plastic strain of the three steels significantly. As expected, for the brittle quasi-cleavage cracking, the evolution of ε_{eqVM} with χ did not follow a logarithm trend as predicted by the Rice and Tracey[50] ductile fracture criterion. For these cases, we considered only a critical pressure necessary for the fracture opening, leading to the representation of the equivalent plastic strain as a function of the hydrostatic stress (σ_m) as seen in the Figure 8(b.i). This graph shows the decrease of σ_m and ε_{eqVM} with the applied cathodic current density at the entry side of the permeation test. Interestingly, the relationships between ε_{eqVM} and σ_m are dependent on the specimen geometry but with similar behavior for the Ref, HMV and HCV steels. The representation of σ_m as a function of the permeation flux (from the measured anodic current at the exit side) is also provided in the Figure 8(b.ii). The results of Figure

8(b.ii) show sharp decreases of σ_m for the lowest values of permeation flux, followed by plateaus where the hydrostatic stress to fracture evolved very little with the values of permeation hydrogen flux. The U specimens presented the highest embrittlement levels (reductions of $\sigma_{m)}$ compared to the specimens tested in air (J = 0) and the Kt 1.1 specimens had a more progressive decrease of σ_m as the hydrogen flux increased.

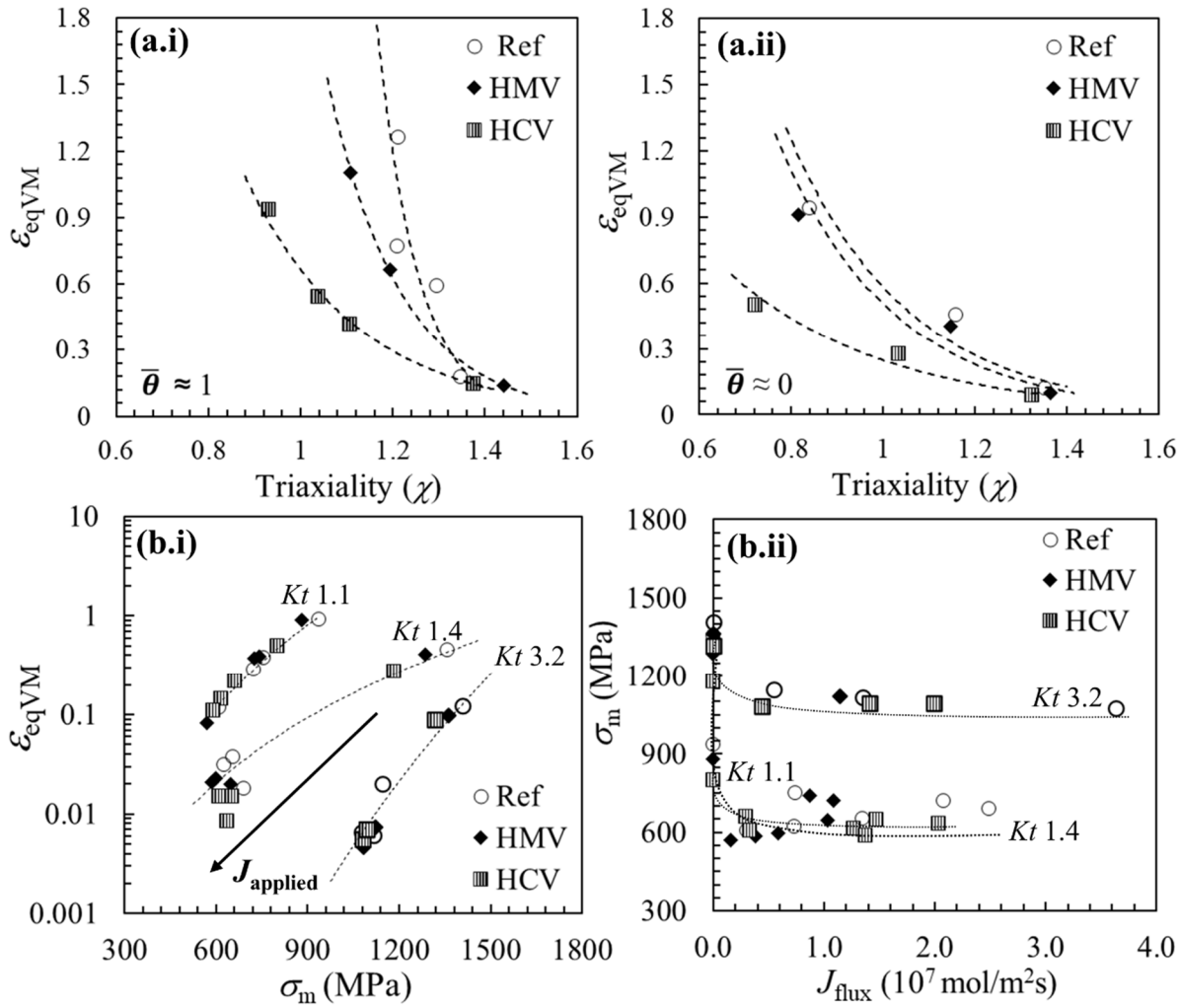

Figure 8: Computed failure criterion for (a) ductile fracture without mobile hydrogen of (a.i) round and (a.ii) flat specimens, (b) QC cracking under hydrogen flux in terms of (b.i) ε_{eqVM} and hydrostatic stress, and (b.ii) hydrostatic stress and permeation hydrogen flux.

Afterwards, the calculations were incremented with hydrogen diffusion driven by hydrostatic stress variations besides the concentration gradients according to the diffusion and trapping equations explained previously in the section 2.3. This approach aimed to consider the impact

of the notches in the distribution of diffusible hydrogen. Firstly, two computations (a mechanical and a diffusion one) were performed to provide the distributions of hydrostatic stress, diffusible hydrogen concentration and apparent diffusion coefficient, which are the initial conditions for a next step that obtain the hydrogen redistribution. For the diffusion computations, the boundary conditions were the experimental C_0 value constant at the entry surface, whereas a C_D constant value equal to 0 at the exit surface. Figure 9 provides an example of calculation results for a V-notched specimen of the HCV steel tested with 50 mA/cm^2, showing the distributions of σ_m and ε_{peq} at the fracture and the redistributions of hydrogen after 3000s of diffusion coupled with hydrostatic stress gradient. The choice of 3000s corresponds to the average time of the tensile tests until fracture for the U and V notched specimens, although it was noticed that the distributions did not change much after 2000s of coupled diffusion. The computed distributions are shown throughout the specimen thicknesses (x). The location where $x = 0$ corresponds to the middle of the thickness, $x < 0$ half the specimen where hydrogen is introduced at the entry surface and $x > 0$ half the specimen where hydrogen is drained from the exit surface, as represented in the colored map of diffusible hydrogen concentration. Additionally, a fracture surface image with the depth of the QC regions is shown in Figure 9. This depth is also represented in the graph of the coupled hydrogen distribution as a dashed black line. The coupled hydrogen diffusion computations provided distinct results for each specimen geometry. The *Kt* 1.1 specimens were modeled in 2D with no notches on the surface apart from a little thickness reduction in order to promote necking. There were only variations of σ_m smaller than 40 MPa throughout the thickness, since the fracture criterion for these specimens was placed just before or just after the necking, with negligible reductions of section. The results of coupled diffusion were then decreasing hydrogen concentration and only minor changes in the flux throughout the thickness (around 1 x 10^{-7} mol/m^{2}s). For the U specimens, the σ_m gradient resulted in a

hydrogen accumulation at the entry surface. Therefore, near the charging side the flux was governed by the hydrostatic stress, whereas closer to the exit surface the flux was governed by the gradient of concentration. The combination of these components resulted in a flux nearly constant throughout the thickness, slightly higher than the ones before coupling. Finally, the V specimens had the biggest derivatives of σ_m resulting in important hydrogen concentration and flux peaks at the hydrogen entry sub-surfaces.

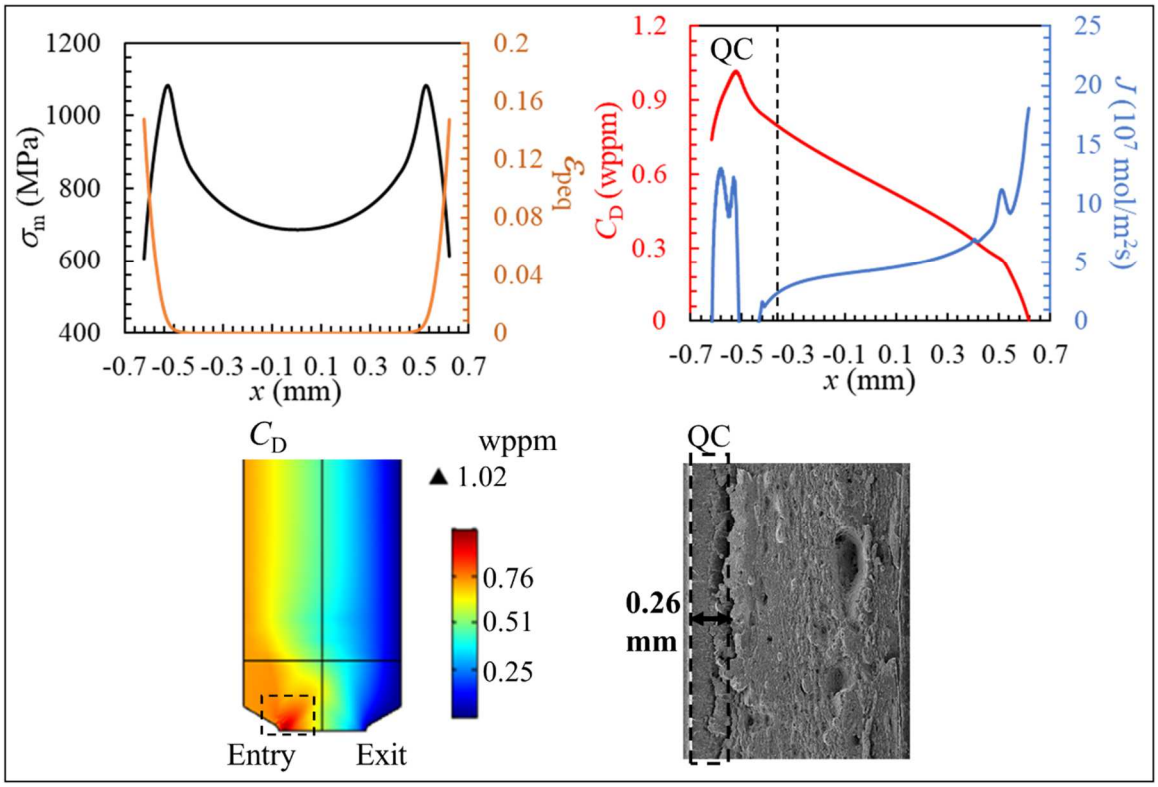

Figure 9: Distributions of modeled σ_m and ε_{peq}, coupled calculated C_D and J through the specimen thickness (x, where $x = 0$ corresponds to the middle of the thickness), colored map of coupled C_D and fracture surface showing the depth of the QC zone at the hydrogen entry surface for the V-notched specimen of the HCV steel tested with 50 mA/cm^2. Dashed line indicated the border of the QC region at the hydrogen entry surface.

The local distributions of flux ($J_{flux\ loc}$) and diffusible hydrogen concentration ($C_{D\ loc}$) allowed reviewing the representation of the QC fracture criterion in terms of ε_{eqVM} and local peak maximum principal stress (σ_1) as can be seen in Figure 10. In the chart of Figure 10(a), there is a great dispersion in the ε_{eqVM} values preventing distinguishing the behavior of the three steels. Most of the ε_{eqVM} values appear to reduce with $C_{D\ loc}$ up to ε_{eqVM} around 0.005. On the

other hand, the tendencies of Figure 10(b) are less dispersed. Similar to previous works based on slow strain rate testing (SSRT) of hydrogen pre-charged notched specimens[31-32], Figure 10(b) displays a failure locus in terms of reduction of local peak maximum principal stress (σ_I) with local diffusible hydrogen concentration ($C_{D\ loc}$) for the three notch geometries represented by their *Kt* values. These decreases of the failure stress are very sharp reaching plateaus for very low concentrations where σ_I is nearly independent of $C_{D\ loc}$. In this figure, the data of the three steels are plotted together since it was not possible to observe differences between their QC fracture criteria, although they presented differences in hydrogen diffusion (Table 3) and in ductile fracture resistance (Figure 8[a]). This result indicates that the stress states inside the specimens have a higher impact in the computed local values of diffusible hydrogen concentration and flux than the hydrogen diffusion kinetics of the steels.

It is also possible to observe from Figure 10(b) that there is a similar failure curve for the specimens with *Kt* 1.1 and 1.4 and another one with higher local stress for the V ones. These differences could be related to the contribution of plastic strain to the QC cracking. In order to verify it, Figure 10(c) shows a 3D plot of failure criterion in terms of failure stress (σ_I), $C_{D\ loc}$ and ε_{eqVM}. It is possible to see in this chart that although some specimens with *Kt* equal to 1.1 have higher values of fracture plastic strain, the contribution of ε_{eqVM} does not seem to justify all the lower values of failure stresses, especially for U specimens (*Kt* = 1.4) presenting negligible local fracture ε_{eqVM} values when tested under hydrogen flux (between 0.008 and 0.04), slightly above the ones of the V specimens (between 0.005 and 0.02).

Finally, a brief analysis of crack propagation was performed by calculating the stress intensity factors (K_I) reached for shifting from QC cracking towards ductile propagation mode. These K_I values were estimated by Equation 9 where "*a*" is the QC crack length measured from the fracture surfaces and *Y* a geometrical correction factor considered equal to 1.12. For the *Kt* 1.1 specimens, the QC zones are approximately semi elliptical. Under uniaxial loading, the

maximum K_I is at the deepest point of the crack and Y is equal to 1.12 considering the ellipse major axis much larger than the minor axis. For the U and V specimens, we took into consideration the notch effect by using the local computed highest principal stress at the QC/ductile transition as σ in the calculation according to the Equation 9.[52]

$$K_I = \sigma Y \sqrt{\pi a} \quad (9)$$

Figure 10(d) shows the evolutions of all the calculated K_I values with the computed local diffusible hydrogen concentration. The values range between 15 and 55 MPam$^{1/2}$. In the absence of hydrogen, the plane-strain fracture toughness (K_{IC}) for ductile fracture of martensitic steels is often above 100 MPam$^{1/2}$.[53-54] The K_I values of the present work indicate that there is a considerable effect of hydrogen flux on promoting cracking of the studied steels. Decrease of K_I due to diffusible hydrogen was already observed for the AERMET martensitic steel, in which the microvoids fracture toughness (K_{IC}) reduced from values around 140 MPa m$^{1/2}$ to threshold K_I values as low as 12 MPam$^{1/2}$ due to diffusible hydrogen.[53]

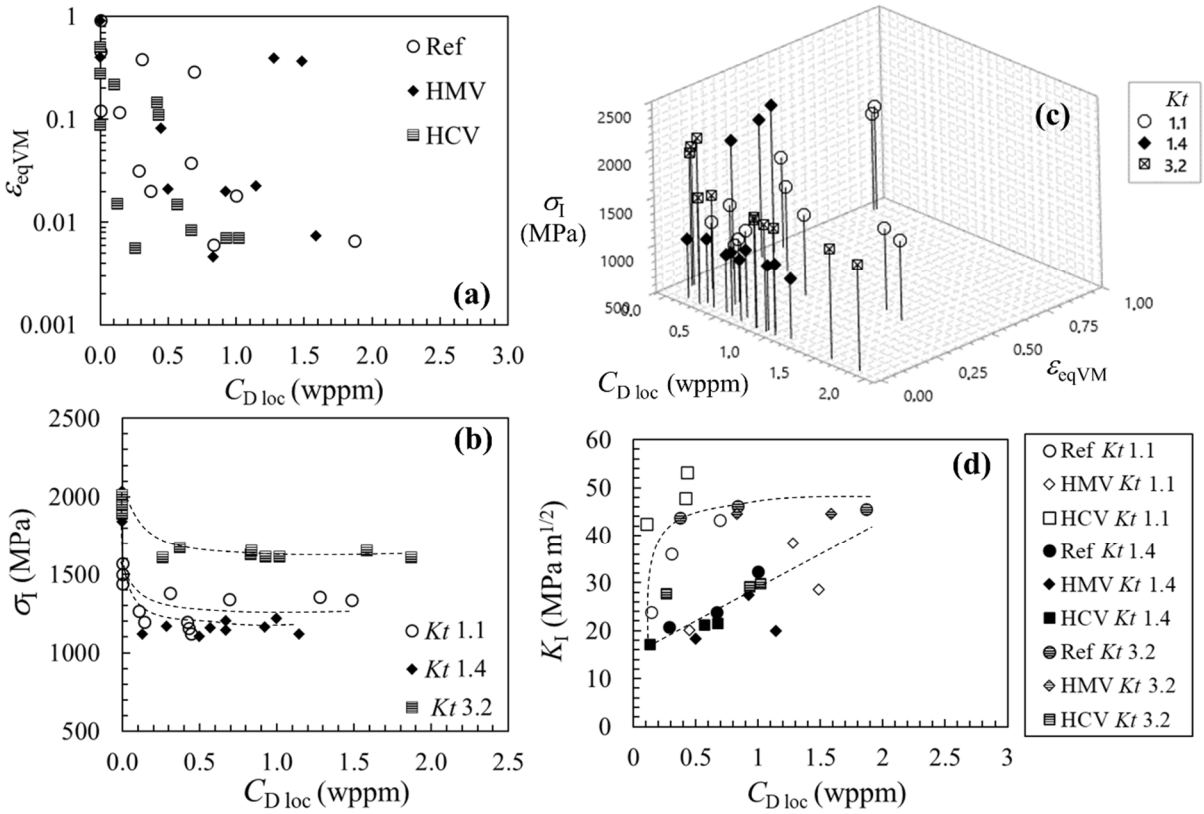

Figure 10: Computed local fracture criterion in terms of (a) ε_{eqVM} and diffusible hydrogen concentration ($C_{D\,loc}$), (b) maximum principal stress (σ_I) and $C_{D\,loc}$, (c) σ_I, $C_{D\,loc}$ and ε_{eqVM}. (d) Summary of K_I values as a function of $C_{D\,loc}$.

Figure 10(d) also reveals that the geometry of the specimens and the metallurgy play an important role with lower K_I values for all U (Kt = 1.4) specimens and higher K_I values for the V (Kt = 3.2) Ref and HMV specimens and some Kt =1.1 specimens, especially for the HCV steel. Additionally, there is a global tendency of increasing K_I values with $C_{D\,loc}$ (also with hydrogen flux, $J_{flux\,loc}$) for values lower than 1.5 wppm. These smaller values of K_I for lower hydrogen concentration are the opposite from what expected, which is a decrease of the threshold K_I values with the diffusible hydrogen concentration.[53, 55-56] It is difficult to explain this discrepancy, but we believe it is related to the test methodology and the effect of plastic strain. In this work, K_I evaluates ductile propagations after brittle transgranular QC cracks for distinct specimen geometries. Therefore, it does not correspond exactly to the threshold K_I for hydrogen stress cracking usually obtained by standard laboratory methods using the stress necessary to crack propagation of pre-cracked specimens.

4. Discussion

This work evaluated the effect of hydrogen on fracture of three tempered martensitic steels by performing uniaxial tensile tests until fracture with round notched specimens in air and after hydrogen pre-charging and desorption along with tests using flat notched specimens in air and under hydrogen permeation flux. Thereafter, the cracking mechanisms and local fracture conditions were investigated by means of fracture surface imaging and FEM computations.

In the present research, trapped hydrogen did not affect the tensile curves and the fracture surfaces remained entirely ductile as those carried out without hydrogen (Figure 2), even for the superior values of *Kt* (V-notch) and concentration up to 2.6 wppm for the HMV steel. A bimodal distribution of microvoids related to inclusions and carbides were observed for all round specimens in air and hydrogen pre-charged. Different from a previous work where trapped hydrogen increased the voids sizes,[11] trapped hydrogen did not seem to favor dimples nucleation and growth in the present work, with no noticeable change on the dimple sizes. The computation of the local fracture stress and plastic strain revealed differences between the resistance of the steels to microvoids coalescence (Rice and Tracey criterion),[50] with smaller fracture values of von Mises equivalent plastic strain and triaxiality for the HCV steel (Figure 8[a]).

On the other hand, agreeing with several previous works,[11,53,57-59] diffusible hydrogen caused more embrittlement to the steels than the trapped one, promoting earlier failure and changing the fracture from ductile to brittle quasi-cleavage for all the specimen geometries and applied cathodic polarizations for the three studied steels. The effect of hydrogen on the tensile curves varied according to the geometry of the specimens (Figure 4). For the *Kt* 1.1, without notches at the hydrogen entry and exit sides, hydrogen flux reduced considerably the elongation and reduction of section, without affecting the stress values before necking. In contrast, for U (*Kt* 1.4) and V (*Kt* 3.2) specimens tested under hydrogen flux, the tensile curves presented losses

of ductility and strength, which in some cases became more severe as the applied cathodic polarization increased. There were sharp decreases of stress after the maximum engineering values with no hardening, suggesting the occurrence of crack propagation. Afterwards, this development of cracking around the maximum engineering stress was confirmed in the interrupted test of Figure 6.

In our previous study with a tempered martensitic steel with lower yield strength and faster hydrogen diffusion,[11] quasi-cleavage zones appeared at the regions of the specimens where the hydrostatic stress and plastic strain were maximum: at both notch tips for V specimens and around the mid-thickness for the U ones. Interestingly, by performing the same tests under permeation hydrogen flux in the present work, the three studied steels had QC crack initiations at the hydrogen entry surfaces (Figure 5[a]) for all specimen geometries. Cracking initiated at the hydrogen charging surfaces even for U specimens where the local stress and plastic strain states are superior at the bulk. Two microstructural features appear to be related to the quasi-cleavage development. The presence of inclusions or undissolved carbo-nitrides, in which were observed quasi-cleavage fish-eyes similar to the work of Rehrl *et al*.[22] and martensitic boundaries. Multiple cracks were observed in the charging surfaces, some at scale of the martensitic packets and blocks (a few microns) for all the tested conditions. Additionally, the finer microstructure, the smaller quasi-cleavage features (Figure 5[b]). This result and other earlier studies,[7,8,11,16,19] suggest that quasi-cleavage fracture surface develops with decohesion of martensitic boundaries.

The results issued from the elasto-plastic computations aimed to identify local failure criteria for the steels. As expected, mobile hydrogen reduced the fracture local plastic strain and stress. However, it was surprising that no clear differences were observed between the local fracture stress and plastic strain under hydrogen flux between the three studied steels (Figures 8[b]), although they have different resistances to ductile fracture (Figure 8[a]) and hydrogen

diffusion kinetics (Table 3). The computations including hydrogen diffusion coupled with stress distribution have shown that hydrostatic stress gradients change the distribution of hydrogen in notched specimens significantly. U and even more V notches favor hydrogen concentration at the hydrogen entry surface. Unnotched and U specimens had near constant flux distribution, whereas V ones had flux peaks at the entry and exit surfaces. The values from these calculations were used to establish local QC fracture criterion for the steels expressed in Figure 10 in terms of decays of local fracture equivalent plastic strain and/or maximum principal stress with local diffusible hydrogen concentration (it could also be represented in terms of local hydrogen flux, $J_{\text{flux loc}}$). When considered only the decay of $\varepsilon_{\text{eqVM}}$ (10[a]), the values are very dispersed for the three steels, with mobile hydrogen reducing the fracture plastic strain up to negligible values of 0.005. On the other hand, when representing the criterion in terms of decay of fracture stress (10[b]), the values are less dispersed but with no differences between the steels. The fact that a single fracture curve could not be obtained for all the specimen geometries, with higher fracture stress values for the V-notch ones, indicates that these computed failure criteria are not complete. Thereafter, the representation with both fracture plastic strain and stress (10[c]) could not also explain the differences between the specimen geometries, especially for the U-notched ones with negligible local plastic strain and smaller values of fracture stress. The observed cracks at the hydrogen entry surfaces may justify the differences between the local fracture criteria of the specimens (Figures 8[b.ii] and 10[b]), since the mechanical states at the crack tips and the hydrogen accumulation due to them are not included in the models employed in the present work. Finally, the similar QC fracture criteria of the steels might indicate that the resistance to the decohesion of interfaces and crack germination and growth at the surfaces being charged with hydrogen are more important to the resistance to hydrogen-assisted cracking of the studied

steels than the diffusion and trapping behavior in their interior, or their fracture resistance in the absence of hydrogen.

In summary, all the results of the present work regarding fracture under permeation flux led to the conclusion that hydrogen-assisted quasi-cleavage cracking in the studied martensitic steels initiated due to the decohesion of interfaces at the surfaces being charged with hydrogen, containing the highest diffusible hydrogen concentration moving inwards the bulk of the steels. The fracture morphologies of these tests, with brittle initiation at the charging surface followed by ductile propagation perpendicular to the applied stress, are similar to those observed when SSC occurs in hydrogen sulfide-containing environments during standard tests with maintained tensile loading.[60-61] The transition between these two fracture modes depended on the coupling of the mechanical states modified by the notch geometries or structural heterogeneities with the diffusible hydrogen concentration and/or flux (Figure 10[d]). Agreeing to what proposed by Crolet[62] that SSC initiates at cropping out grains with right orientations, the crack threshold conditions in the present study appear to be related to the decohesion of these interfaces. This decohesion could be facilitated at boundaries where dislocation glide occur with hydrogen drag.[25,62] The hydrogen transport by dislocations is not considered in the present study computations but may in fact facilitate the hydrogen concentration and decohesion of interfaces.[26-28] Evidences of hydrogen-plasticity interactions were observed in this work with hardening peaks at the same time of the anodic current peaks at the Lüders plateaus, suggesting that hydrogen can interfere in the slip bands propagation. Additionally, plastic strain caused considerable trapping observed by decreases of hydrogen flux at the permeation exit surface (Figure 7) and by increases of trapped hydrogen concentration measured by TDS after fracture (Figure 3) agreeing with previous works.[34,63]

The methodology of the present work approached in service conditions where high-strength steel structures are being constantly charged with hydrogen and embrittled in their inner

surfaces while desorption can occur at the outer surfaces. This resistance to QC cracking at hydrogen charging surfaces could not be evaluated by usual tests with pre-charged specimens and coatings blocking the hydrogen desorption at the surfaces.[13,29-31] Further research with crack propagation computations incorporating the effect of hydrogen in reducing the cohesion of martensitic boundaries is recommended to obtain more precise local fracture criteria and classify the steels according to their hydrogen-assisted cracking resistance.

5. Conclusions

Hydrogen-assisted quasi-cleavage cracking has been investigated by fracturing unnotched and notched specimens under hydrogen flux in an electrochemical permeation device built on a Instron tensile testing machine. Considerable hydrogen embrittlement was not observed when only trapped hydrogen was present. In contrast, mobile hydrogen reduced the fracture stress and strain promoting quasi-cleavage cracking at the permeation charging surfaces. Multiple cracks at these surfaces ranging from few to hundreds of microns suggest that diffusible hydrogen favor decohesion of interfaces, which happened in some cases around inclusions and undissolved carbides. Although the three studied steels present distinct resistance to ductile microvoids fracture and hydrogen diffusion kinetics, they presented similar resistance to quasi-cleavage cracking when tested under hydrogen flux. The computations coupling hydrogen diffusion with hydrostatic stress gradients predicted local failure criteria for the steels in terms of decays of fracture maximum principal stress and/or equivalent plastic strain with diffusible hydrogen concentration. However, the employed model was not sufficient to predict a single failure criterion for the steels. Therefore, the results of this work indicate that the resistance of the studied martensitic steels to quasi-cleavage depends on the interactions between mobile hydrogen with the entry surface mechanical states and the consequent surface evolutions generating cracking nucleation and propagation. Further modeling should then include mechanical states at the entry surfaces and sub-surfaces, hydrogen flux and

concentration in them with consequent decrease of cohesive energy of boundaries in addition to hydrogen-dislocations interactions ahead nucleated crack tips.

Acknowledgements

The authors thank E. Conforto and G. Lotte for their contributions at the microscopy center facilities of the laboratory LaSIE.

Funding sources

This research did not receive any specific grant from funding agencies in the public, commercial, or not-for-profit sectors.

Data availability

The raw data required to reproduce these findings are available to download from [https://data.mendeley.com/datasets/pzhdk9y9jd/1]. The processed data required to reproduce these findings are available to download from [https://data.mendeley.com/datasets/znk4c6znzf/1].

References

1. J.F. Newman, L.L. Shreir, Role of hydrides in hydrogen entry into steel from solutions containing promoters, Corros. Sci. 9 (1969) 631-641. doi.org/10.1016/S0010-938X(69)80117-4
2. R.N. Iyer, I. Takeuchi, M. Zamanzadeh, H.W. Pickering, Hydrogen sulfide effect on hydrogen entry into Iron- A Mechanistic study, Corrosion 46 (1990) 460-468. doi.org/10.5006/1.3585133
3. C.D. Beachem, A new model for hydrogen-assisted cracking (hydrogen "embrittlement"), Metall. Mater. Trans. B 3 (1972) 441-455. doi.org/10.1007/BF02642048
4. J.E. Costa, A.W. Thompson, Effect of hydrogen on fracture behavior of a quenched and tempered medium-carbon steel, Metall. Mater. Trans. A 12 (1981) 761-771. doi.org/10.1007/BF02648340
5. Y.H. Kim, J.W. Morris, The nature of quasicleavage fracture in tempered 5.5Ni steel after hydrogen charging, Metall. Mater. Trans. A 14 (1983) 1883-1888. doi.org/10.1007/BF02645559
6. M. Nagumo, H. Matsuda, Function of hydrogen in intergranular fracture of martensitic steels, Philos. Mag. A 82 (2002) 3415-3425. doi.org/10.1080/01418610208240452
7. A. Nagao, C.D. Smith, M. Dadfarnia, P. Sofronis, I. M. Robertson, The role of hydrogen in hydrogen embrittlement fracture of lath martensitic steel, Acta Mater. 60 (2012) 5182-5189. doi.org/10.1016/j.actamat.2012.06.040

8. A. Nagao, C.D. Smith, M. Dadfarnia, P. Sofronis, I. M. Robertson, Interpretation of Hydrogen-induced Fracture Surface Morphologies for Lath Martensitic Steel, Procedia Mater. Sci. 3 (2014) 1700-1705. doi.org/10.1016/j.mspro.2014.06.274
9. J. Venezuela, Q. Liu, M. Zhang, Q. Zhou, A. Atrens, The influence of hydrogen on the mechanical and fracture properties of some martensitic advanced high strength steels studied using the linearly increasing stress test, Corros. Sci. 99 (2015) 98-117. doi.org/10.1016/j.corsci.2015.06.038
10. T. Das, S.K. Rajagopalan, S. V. Brahimi, X. Wang, S. Yue, A study on the susceptibility of high strength tempered martensite steels to hydrogen embrittlement (HE) based on incremental step load (ISL) testing methodology, Mater. Sci. Eng. A 716 (2018) 189-207. doi.org/10.1016/j.msea.2018.01.032
11. D. Guedes, L. Cupertino Malheiros, A. Oudriss, S. Cohendoz, J. Bouhattate, J. Creus, F. Thébault, M. Piette, X. Feaugas, The role of plasticity and hydrogen flux in the fracture of a tempered martensitic steel: A new design of mechanical test until fracture to separate the influence of mobile from deeply trapped hydrogen, Acta Mater. 186 (2020) 133-148. doi.org/10.1016/j.actamat.2019.12.045
12. R.P. Wei, G.W. Simmons, A technique for determining the elemental composition of fracture surfaces produced by crack growth in hydrogen and in water vapor, Scripta Metall., 10 (1976) 153 -157. doi.org/10.1016/0036-9748(76)90138-1
13. P. Novak, R. Yuan, B.P. Somerday, P. Sofronis, R.O. Ritchie, A statistical, physical-based, micro-mechanical model of hydrogen-induced intergranular fracture in steel, J. Mech. Phys. Solids 58 (2010) 206-226. doi.org/10.1016/j.jmps.2009.10.005
14. A. Nagao, M. Dadfarnia, B.P. Somerday, P. Sofronis, R.O. Ritchie, Hydrogen-enhanced-plasticity mediated decohesion for hydrogen-induced intergranular and "quasi-cleavage" fracture of lath martensitic steels, J. Mech. Phys. Solids 112 (2018) 403-430. doi.org/10.1016/j.jmps.2017.12.016
15. J.E. Costa, A.W. Thompson, Effect of hydrogen on fracture behavior of a quenched and tempered medium-carbon steel, Metall. Mater. Trans. A 12 (1981) 761-771. doi.org/10.1007/BF02648340
16. A. Shibata, H. Takahashi, N. Tsuji, Microstructural and Crystallographic Features of Hydrogen-related Crack Propagation in Low Carbon Martensitic Steel, ISIJ Inter. 52 (2012) 208-212. doi.org/10.2355/isijinternational.52.208
17. R.A. Oriani, P.H. Josephic, Equilibrium aspects of hydrogen-induced cracking of steels, Acta Metall. 22 (1974) 1065-1074. doi.org/10.1016/0001-6160(74)90061-3
18. R.A. Oriani, P.H. Josephic, Equilibrium and kinetic studies of the hydrogen-assisted cracking of steel, Acta Metall. 25 (1977) 979-988. doi.org/10.1016/0001-6160(77)90126-2
19. W.T. Geng, V. Wang, J-X. Li, N. Ishikawa, H. Kimizuka, K. Tsuzaki, S. Ogata, Hydrogen trapping in carbon supersaturated α-iron and its decohesion effect in martensitic steel, Scripta Mater. 149 (2018) 79-83. doi.org/10.1016/j.scriptamat.2018.02.025
20. M. Nagumo, Hydrogen related failure of steels – a new aspect, Mater. Sci. Tech. 20 (2004) 940-950. doi.org/10.1179/026708304225019687
21. M.B. Djukic, V. Sikacki Zeravcic, G. Bakic, A. Sedmak, B. Rajicic, Hydrogen Embrittlement of Low Carbon Structural Steel, Procedia Mater. Sci. 3 (2014) 1167-1172. doi.org/10.1016/j.mspro.2014.06.190
22. J. Rehrl, K. Mraczek, A. Pichler, E. Werner, Mechanical properties and fracture behavior of hydrogen charged AHSS/UHSS grades at high- and low strain rate tests, Mater. Sci. Eng. A 590 (2014) 360-367. doi.org/10.1016/j.msea.2013.10.044

23. H.K. Birnbaum, P. Sofronis, Hydrogen-enhanced localized plasticity—a mechanism for hydrogen-related fracture, Mater. Sci. Eng. A 176 (1994) 191-202. doi.org/10.1016/0921-5093(94)90975-X
24. P.J. Ferreira, I.M. Robertson, H.K. Birnbaum, Hydrogen effects on the interaction between dislocations, Acta Mater. 46 (1998) 1749-1757. doi.org/10.1016/S1359-6454(97)00349-2
25. X. Feaugas, D. Delafosse, Hydrogen and Crystal Defects Interactions: Effects on Plasticity and Fracture in Mechanics - Microstructure - Corrosion Coupling, 1st ed., Elsevier Publisher (2019) 199-222. doi.org/10.1016/B978-1-78548-309-7.50009-0
26. I.-W. Kang, S.-I. Pyun, K.-T. Kim, The effects of dislocations on the trapping and transport of hydrogen in 3.3 Ni - 1.6 Cr steel during plastic deformation, Scripta Metall. 23 (1989) 223-226. doi.org/10.1016/0036-9748(89)90415-8
27. M. Dadfarnia, M.L. Martin, A. Nagao, P. Sofronis, I.M. Robertson, Modeling hydrogen transport by dislocations, J. Mech. Phys. Solids 78 (2015) 511-525. doi.org/10.1016/j.jmps.2015.03.002
28. D. Guedes, A. Oudriss, S. Cohendoz, J. Creus, J. Bouhattate, X. Feaugas, F. Thebault, D. Koschel, The Influence of Hydrogen Flux on Crack Initiation in Martensitic Steels, Procedia Mater. Sci. 3 (2014) 2024-2029. doi.org/10.1016/j.mspro.2014.06.326
29. M. Wang, E. Akiyama, K. Tsuzaki, Effect of hydrogen and stress concentration on the notch tensile strength of AISI 4135 steel, Mater. Sci. Eng. A 398 (2005) 37-46. doi.org/10.1016/j.msea.2005.03.008
30. M.-Q. Wang, E. Akiyama, K. Tsuzaki, Fracture criterion for hydrogen embrittlement of high strength steel, Mater. Sci. Tech. 22 (2006) 167-172. doi.org/10.1179/174328406X86191
31. M. Wang, E. Akiyama, K. Tsuzaki, Effect of hydrogen on the fracture behavior of high strength steel during slow strain rate test, Corros. Sci. 49 (2007) 4081-4097. doi.org/10.1016/j.corsci.2007.03.038
32. C. Ayas, V.S. Deshpande, N.A. Fleck, A fracture criterion for the notch strength of high strength steels in the presence of hydrogen, J. Mech. Phys. Solids 63 (2014) 80-93. doi.org/10.1016/j.jmps.2013.10.002
33. Y. Hagihara, C. Ito, N. Hisamori, H. Suzuki, K. Takai, E. Akiyama, Evaluation of Delayed Fracture Characteristics of High Strength Steel based on CSRT Method, Tetsu-to-Hagane 94 (2008) 215-221. doi.org/10.2355/tetsutohagane.94.215
34. S. Frappart, X. Feaugas, J. Creus, F. Thebault, L. Delattre, H. Marchebois, Hydrogen solubility, diffusivity and trapping in a tempered Fe–C–Cr martensitic steel under various mechanical stress states, Mater. Sci. Eng. A 534 (2012) 384-393. doi.org/10.1016/j.msea.2011.11.084
35. R.K. Ham, The determination of dislocation densities in thin films, The Philosophical Magazine: A Journal of Theoretical Experimental and Applied Physics 6 (1961) 1183-1184. doi.org/10.1080/14786436108239679
36. S. Frappart, X. Feaugas, J. Creus, F. Thebault, L. Delattre, H. Marchebois, Study of the hydrogen diffusion and segregation into Fe–C–Mo martensitic HSLA steel using electrochemical permeation test, J. Phys. Chem. Solids 71 (2010) 1467-1479. doi.org/10.1016/j.jpcs.2010.07.017
37. S. Frappart, A. Oudriss, X. Feaugas, J. Creus, J. Bouhattate, F. Thébault, L. Delattre, H. Marchebois, Hydrogen trapping in martensitic steel investigated using electrochemical

permeation and thermal desorption spectroscopy, Scripta Mater. 65 (2011) 859-862. doi.org/10.1016/j.scriptamat.2011.07.042
38. J.L. Chaboche, A review of some plasticity and viscoplasticity constitutive theories, Inter. J. Plasticity 24 (2008) 1642-1693. doi.org/10.1016/j.ijplas.2008.03.009
39. A.H.M. Krom, A. Bakker, Hydrogen trapping models in steel, Metall. Mater. Trans. B 31 (2000) 1475-1482. doi.org/10.1007/s11663-000-0032-0
40. J. Huez, A.L. Helbert, X. Feaugas, I. Guillot, M. Clavel, Damage process in commercially pure α-titanium alloy without (Ti40) and with (Ti40-H) hydrides, Metall. Mater. Trans. A 29 (1998) 1615-1628. doi.org/10.1007/s11661-998-0085-2
41. D. Guedes, A. Oudriss, S. Frappart, G. Courlit, S. Cohendoz, P. Girault, J. Creus, J. Bouhattate, A. Metsue, F. Thebault, L. Delattre, D. Koschel, X. Feaugas, The influence of hydrostatic stress states on the hydrogen solubility in martensitic steels, Scripta Mater. 84-85 (2014) 23-26. doi.org/10.1016/j.scriptamat.2014.04.006
42. P. Sofronis, R.M. McMeeking, Numerical analysis of hydrogen transport near a blunting crack tip, J. Mech. Phys. Solids 37 (1989) 317-350.doi.org/10.1016/0022-5096(89)90002-1
43. A.H.M Krom, R.W.J Koers, A. Bakker, Hydrogen transport near a blunting crack tip, J. Mech. Phys. Solids 47 (1999) 971-992. doi.org/10.1016/S0022-5096(98)00064-7
44. C. Guillemer-Neel, X. Feaugas, M. Clavel, Mechanical behavior and damage kinetics in nodular cast iron: Part II. Hardening and damage, Metall. Mater. Trans. A 31 (2000) 3075-3085. doi.org/10.1007/s11661-000-0086-2
45. R.A. Oriani, The diffusion and trapping of hydrogen in steel, Acta Metall. 18 (1970) 147-157. doi.org/10.1016/0001-6160(70)90078-7
46. L.C. Hwang, T.P. Perng, Hydrogen transport in ferritic stainless steel under elastic stress, Mater. Chem. Phys. 36 (1994) 231-235. doi.org/10.1016/0254-0584(94)90034-5
47. E. Van den Eeckhout, T. Depover, K. Verbeken, The Effect of Microstructural Characteristics on the Hydrogen Permeation Transient in Quenched and Tempered Martensitic Alloys, Metals 8(10) (2018) 779. doi.org/10.3390/met8100779
48. W. Lode, Versuche über den Einfluß der mittleren Hauptspannung auf das Fließen der Metalle Eisen, Kupfer und Nickel, Z. Physik 36 (1926) 913-939. doi.org/10.1007/BF01400222
49. D. Mohr, S.J. Marcadet, Micromechanically-motivated phenomenological Hosford–Coulomb model for predicting ductile fracture initiation at low stress triaxialities, Inter. J. Solids Structures 67-68 (2015) 40-55. doi.org/10.1016/j.ijsolstr.2015.02.024
50. J.R. Rice, D.M. Tracey, On the ductile enlargement of voids in triaxial stress fields, J. Mech. Phys. Solids 17 (1969) 201–217. doi.org/10.1016/0022-5096(69)90033-7
51. P.F. Thomason, A three-dimensional model for ductile fracture by the growth and coalescence of microvoids, Acta Metall. 33 (1985) 1087-1095. doi.org/10.1016/0001-6160(85)90202-0
52. L.P. Pook, Linear Elastic Fracture Mechanics for Engineers: Theory and Applications, 1st ed., WIT Press, Southampton UK (2000) 176.
53. R.L.S. Thomas, J. R. Scully, R. P. Gangloff, Internal hydrogen embrittlement of ultrahigh-strength AERMET 100 steel, Metall. Mater. Trans. A 34 (2003) 327-344. doi.org/10.1007/s11661-003-0334-3
54. Y. Liang, S. Long, P. Xu, Y. Lu, Y. Jiang, Y. Liang, M. Yang, The important role of martensite laths to fracture toughness for the ductile fracture controlled by the strain in EA4T axle steel, Mater. Sci. Eng. A 695 (2017) 154-164. doi.org/10.1016/j.msea.2017.03.110

55. Y. Yamaguchi, H. Nonaka, K. Yamakawa, Effect of Hydrogen Content on Threshold Stress Intensity Factor in Carbon Steel in Hydrogen-Assisted Cracking Environments, CORROSION 53(2) (1997) 147-155. doi.org/10.5006/1.3280452
56. Y. Kim, Y.J. Chao, M.J. Pechersky, M.J. Morgan, On the Effect of Hydrogen on the Fracture Toughness of Steel, Inter. J. Fracture 134 (2005) 339-347. doi.org/10.1007/s10704-005-1974-7
57. W.H. Johnson, II. On some remarkable changes produced in iron and steel by the action of hydrogen and acids, Proc. R. Soc. Lond. 23 (1875) 168-179. doi.org/10.1098/rspl.1874.0024
58. A. Oudriss, A. Fleurentin, G. Courlit, E. Conforto, C. Berziou, C. Rébéré, S. Cohendoz, J.M. Sobrino, J. Creus, X. Feaugas, Consequence of the diffusive hydrogen contents on tensile properties of martensitic steel during the desorption at room temperature, Mater. Sci. Eng. A 598 (2014) 420-428. doi.org/10.1016/j.msea.2014.01.039
59. H.K.D.H. Bhadeshia, Prevention of Hydrogen Embrittlement in Steels, ISIJ Inter. 56 (2016) 24-36. doi.org/10.2355/isijinternational.ISIJINT-2015-430
60. V. Smanio, J. Kittel, M. Fregonese, T. Cassagne, B. Normand, F. Ropital, Acoustic Emission Monitoring of Wet H2S Cracking of Linepipe Steels: Application to Hydrogen-Induced Cracking and Stress-Oriented Hydrogen-Induced Cracking, CORROSION 67(6) (2011) 065002-1–12. doi.org/10.5006/1.3595097
61. H. Tang, M.S. Cayard, Test Methods for Evaluation of Materials for Wet H2S Service, Corrosion NACE Int. 99421 (1999) 421/1-14.
62. J-L. Crolet, Analysis of the various processes downstream cathodic hydrogen charging, IV: detailed mechanism of sulfide stress cracking, Matériaux & Tech. 104 (303) (2016) 1-13. doi.org/10.1051/mattech/2016026
63. K. Takai, H. Shoda, H. Suzuki, M. Nagumo, Lattice defects dominating hydrogen-related failure of metals, Acta Mater. 56 (2008) 5158-5167. doi.org/10.1016/j.actamat.2008.06.031
64.